ANNUAL REVIEWS

Annual Review of Astronomy and Astrophysics

Relativistic Jets from Active Galactic Nuclei

Roger Blandford,[1] David Meier,[2,3] and Anthony Readhead[4]

[1]Kavli Institute for Particle Astrophysics and Cosmology, Stanford University, Stanford, California 94305, USA: email: rdb3@stanford.edu

[2]Department of Astronomy, California Institute of Technology, Pasadena, California 91125, USA

[3]Jet Propulsion Laboratory, Pasadena, California 91109, USA

[4]Owens Valley Radio Observatory, California Institute of Technology, Pasadena, California 91125, USA

Annu. Rev. Astron. Astrophys. 2019. 57:467–509

The *Annual Review of Astronomy and Astrophysics* is online at astro.annualreviews.org

https://doi.org/10.1146/annurev-astro-081817-051948

Copyright © 2019 by Annual Reviews. All rights reserved

ANNUAL REVIEWS CONNECT

www.annualreviews.org

- Download figures
- Navigate cited references
- Keyword search
- Explore related articles
- Share via email or social media

Keywords

active galactic nuclei, black holes, jets, extragalactic radio sources, γ-ray sources, blazars

Abstract

The nuclei of most normal galaxies contain supermassive black holes, which can accrete gas through a disk and become active. These active galactic nuclei (AGNs) can form jets that are observed on scales from astronomical units to megaparsecs and from meter wavelengths to TeV energies. High-resolution radio imaging and multiwavelength/messenger campaigns are elucidating the conditions under which this happens. Evidence is presented that:

- Relativistic AGN jets are formed when the black hole spins and the the accretion disk is strongly magnetized, perhaps on account of gas accreting at high latitude beyond the black hole sphere of influence.
- AGN jets are collimated close to the black hole by magnetic stress associated with a disk wind.
- Higher-power jets can emerge from their galactic nuclei in a relativistic, supersonic, and proton-dominated state, and they terminate in strong, hot spot shocks; lower-power jets are degraded to buoyant plumes and bubbles.
- Jets may accelerate protons to EeV energies, which contribute to the cosmic ray spectrum and may initiate pair cascades that can efficiently radiate synchrotron γ-rays.
- Jets were far more common when the Universe was a few billion years old and black holes and massive galaxies were growing rapidly.

- Jets can have a major influence on their environments, stimulating and limiting the growth of galaxies.

The observational prospects for securing our understanding of AGN jets are bright.

Contents

1. INTRODUCTION

A curious straight ray lies in a gap in the nebulosity in p.a. 20°, apparently connected with the nucleus by a thin line of matter. The ray is brightest at its inner end, which is 11″ from the nucleus.

—H.D. Curtis [1918, p. 31, description of a 5-min exposure of NGC 4486 (M87)]

1.1. Historical Context

As the above quotation attests, jets were first observed more than a century ago. Much has been learned since then through the application of new technology, which enabled remarkable gains in sensitivity and angular and spectral resolution and which has revealed jets throughout the entire electromagnetic spectrum as well as the gravitational, and perhaps neutrino and cosmic ray, windows. Simultaneously, understanding of relativity, quantum mechanics, and the physics of ionized gas provided a secure foundation to interpret these observations.

Fath (1909) produced the first manifestation of an active galactic nucleus (AGN) but it was not until Seyfert (1943) that the presence of a central gravitational well was suggested, in retrospect, by the observation of broad emission lines from gas moving at high speed. Radio astronomy began in the 1930s (Jansky 1933, Reber 1944). A key discovery was the resolution of a bright radio source, Cygnus A, into two components or lobes (Jennison & Das Gupta 1953) straddling a galaxy at a redshift $z \sim 0.05$ (Baade & Minkowski 1954). Synchrotron radiation was identified as the radio emission mechanism and shown to require enormous energies (Shklovsky 1955, Burbidge 1956). The first quasar, 3C273, was discovered in 1963 (Hazard et al. 1963, Schmidt 1963) and shown to have a radio power [$L_{\rm rad} \equiv {\rm d}L/{\rm d}\ln\nu(6\,{\rm GHz})$], with L the luminosity, even greater than Cygnus A. It had a compact flat radio spectrum core, with spectral index $\alpha \equiv {\rm d}\ln L/{\rm d}\ln\nu \sim 0$ and a linear jet extending to 20 arcsec, very similar to that in M87. The spectrum of 3C273 was distinguished from that of Cygnus A by the presence of broad, as opposed to narrow, emission lines, which is a distinguishing feature between radio galaxies and quasars. Another distinguishing feature is that the radio sources associated with radio-loud quasars (RLQs) are often compact, whereas those associated with radio galaxies are extended, although most RLQs large enough to be resolved show the same double-lobe morphology as radio galaxies.

AGNs were observed throughout the electromagnetic spectrum. The historical optical magnitude and the contemporary radio flux of 3C273 varied dramatically on timescales of days to years (Smith & Hoffleit 1963, Dent 1965). More generally, blazars were found to be highly variable in the radio (Hughes 1965), optical (Schmidt 1963), X-ray (Schreier et al. 1982) and γ-ray (Bignami 1981, Punch et al. 1992) bands, on timescales that can be as short as minutes. Radio-quiet quasars (RQQs) were found in optical surveys and shown to be roughly ten times more numerous than RLQs and just as powerful in the optical (Sandage 1965). Before long it became clear that most normal galaxies have nuclei which can be identified through their spectral lines, stellar activity or nonthermal emission (Keel 1983). This includes our own Galaxy, for which the nucleus Sgr A* (Balick & Brown 1974) has a radio luminosity $L_{\rm rad} \sim 10^{33}\,{\rm erg\,s^{-1}} \sim 10^{-3}L_{\rm bol}$, with $L_{\rm bol}$ being the bolometric luminosity.

Theory, viewed selectively, kept up with these remarkable discoveries. Some early models of quasars (Salpeter 1964, Zel'dovich & Novikov 1964) correctly invoked supermassive black holes (SMBHs), largely to account for the high radiative efficiency. Accretion disks (Lynden-Bell 1969, Bardeen 1970) were investigated, and double radio sources were seen to be powered continuously by jets emanating from galactic nuclei (Rees 1971), rather than as remnants of single explosions like supernovae. Their rapid radio variability led Rees (1966) to propose relativistic motion in RLQs. This suggestion—that relativistic motion, with its concomitant angular beaming effects, dominates the observed characteristics of RLQs—was the first critical step toward unifying flat-spectrum radio quasars (FSRQs) with radio galaxies (mostly steep spectra). It also alleviated the physical challenges posed by compact radio sources (Hoyle et al. 1966). Generic particle, fluid, and electromagnetic models of jets were explored to account for their origin, collimation, and radiation (Blandford & Rees 1974, Scheuer 1974).

Active galactic nucleus (AGN): compact region at the center of a galaxy with high, nonstellar luminosity

Quasar: an AGN that outshines its host galaxy

Radio-loud quasar (RLQ): quasar with $10^{40}\,{\rm erg\,s^{-1}} < L_{\rm rad} \lesssim 10^{46}\,{\rm erg\,s^{-1}}$

Blazar: AGN with relativistic jet directed toward us

Radio-quiet quasar (RQQ): quasar with $10^{38}\,{\rm erg\,s^{-1}} \lesssim L_{\rm rad} < 10^{40}\,{\rm erg\,s^{-1}}$

Supermassive black hole (SMBH): spinning black hole with mass in the range $\sim 10^{6-10}\,{\rm M}_\odot$

Flat-spectrum radio quasar (FSRQ): high-power blazar with quasar properties

1.2. This Review

In preparing this review on AGN jets, we have chosen to emphasize topics where there has been recent progress or where we judge it to be imminent. Much of this activity involves multiwavelength and messenger investigations of AGNs in general. The research literature is therefore immense—maybe a thousand citable references per year—and we have had to make ruthless choices to keep this review within editorial bounds. We have chosen to emphasize papers that either give a clear context to the research, provide instructive examples of more general jet properties, or connect well to upcoming investigations. We eschew references where extensive discussion can be easily found on websites. Consequently, many important technical advances, discoveries, ideas, and detailed studies can only be recognized implicitly. To those involved, we offer sincere apologies.

The following section contains an overview of direct observations of jets together with relevant discussion of the black holes and accretion disks that launch them and the radio lobes that they feed. Section 3 deals with kinematic and dynamical inferences that have been drawn from these observations. Jets are mostly observed nonthermally, which requires relativistic particles to be accelerated and radiation mechanisms to be identified. We discuss these matters in Section 4 and turn to the relationship of jets to AGNs and the Universe at large in Section 5. Finally, in Section 6, we summarize our view of what is reasonably well-established about AGN jets and list some important open issues that should be elucidated over the next decade using new telescopes. S.W. Davis and A. Tchekhovskoy (submitted) provide a complementary discussion of numerical simulations of accretion disks and jets.

2. OBSERVATIONS OF RELATIVISTIC JETS

"We shall call this 'superlight expansion.'"

—M.H. Cohen et al. (1971, p. 215)

2.1. Background

We can now count $\sim 10^9$ extragalactic radio sources, mostly with $L_{\rm rad} \gtrsim 10^{38}\,{\rm erg\,s^{-1}}$ (comparable with the Milky Way), in low-frequency radio surveys. A substantial fraction of these sources are cores, jets, and lobes powered by SMBHs; the remainder are dominated by stellar processes. (Padovani 2016). The observation and theory of SMBH sources were reviewed by Bridle & Perley (1984), Begelman et al. (1984), and Rees (1984). While there has been much progress and many fine reviews since, the early results provide a convenient starting point for much of our discussion.

2.1.1. Unified theories. The early radio surveys were all carried out at frequencies of a few hundred MHz, and although individual sources were followed up at higher frequencies, the low-frequency surveys led to a strong focus on steep spectrum sources, since these objects predominate at low frequencies. In a seminal paper, Kellermann & Pauliny-Toth (1969) drew attention to the importance of flat-spectrum sources, but it was not until the S surveys (Pauliny-Toth et al. 1978) produced a complete sample of 771 radio sources at 5 GHz that the importance of the flat-spectrum sources was fully recognized. Of the strong (>0.6 Jy) radio sources selected at 5 GHz, $\sim$55% are compact (<1 arcsec) flat-spectrum objects, predominantly quasars, while $\sim$45% are extended (>1 arcsec) steep spectrum objects, predominantly galaxies (Pauliny-Toth et al. 1978). This was an important result because it provided a key ingredient to theories that unified radio galaxies and quasars. In one of the largest radio galaxies, NGC 6251, the parsec-scale jet was found to be parallel to, and pointing in the same direction as, the 200-kpc jet (Readhead et al. 1978a). This result, coupled with the flat/steep spectrum radio source

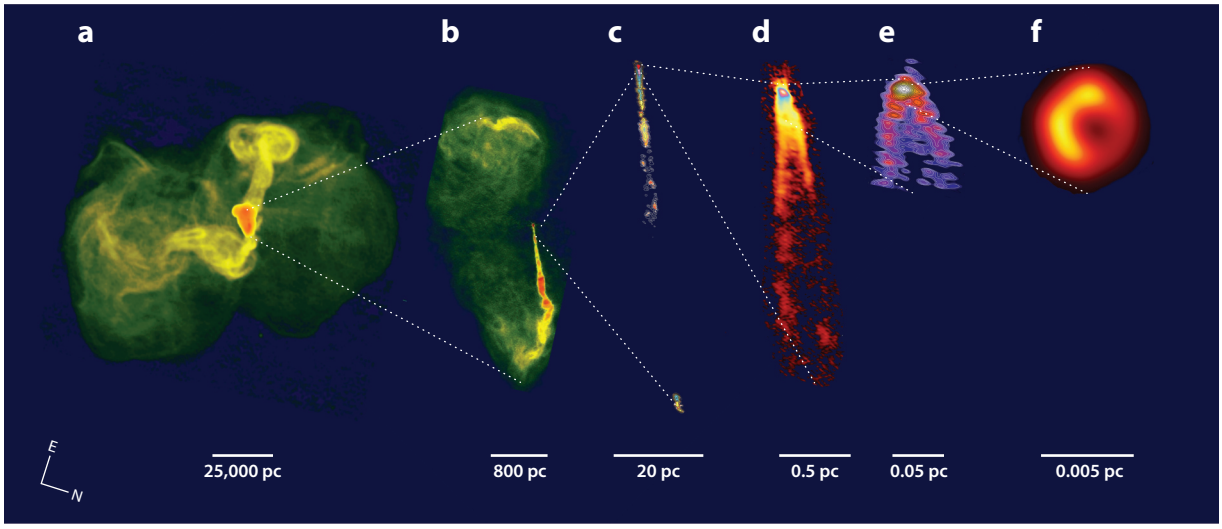

Figure 1

Montage of the FR-I radio galaxy M87 on scales from the outer lobes to near the black hole. (*a*) Lobe jet and outer lobes, showing the present outburst and a more ancient one almost perpendicular to the former; (*b*) galaxy jet and inner lobes; (*c*) full view of the black hole jet, including the prominent optical feature HST-1 at $R_{\rm inf}$ (see Section 2.2.1); (*d*) innermost jet; (*e*) jet launching region near supermassive black hole; and (*f*) inner accretion disk and black hole. Images *b*–*d* show the striking effects of relativistic beaming, even with the jet pointing at an angle ∼17° to our line of sight (Walker et al. 2018). The counter-jet is largely invisible, pointing away from us at an angle ∼163°. Images adapted with permission from (*a*) NRAO, 90-cm VLA; (*b*) NRAO, 20-cm VLA; (*c*) NRAO, 20-cm VLBA (Cheung et al. 2007); (*d*) NRAO, 7-mm VLBA (Walker et al. 2018); (*e*) 3-mm global VLBI network (Kim et al. 2018); (*f*) 1.3-mm Event Horizon Telescope (EHT Collab. 2019) image of accretion disk and supermassive black hole. Abbreviations: FR-I, Fanaroff–Riley type 1; VLA, Very Large Array; VLBA, Very Long Baseline Array; VLBI, very long baseline interferometry.

dichotomy, and superluminal motion, led Readhead et al. (1978b) to suggest relativistic beaming (see **Figure 1**) and orientation (Rees 1966) as the possible reasons for the apparent differences at radio wavelengths between these two classes—viz. flat/steep spectra, compact/extended structure, misaligned/aligned with larger-scale structure, superluminal/absence of superluminal motion (see the sidebar titled Special Relativistic Effects).

Blandford & Rees (1978) extended these arguments to BL Lac objects (BLLs), and Blandford & Königl (1979) and Königl (1981) presented theoretical discussions of relativistic jets as compact radio, X-ray and γ-ray sources. Over the next two years the results continued to strengthen the case for unified theories (Readhead 1980, Orr & Browne 1982). The results favoring a powerful unifying theory were summarized by Begelman et al. (1984), but there was one major piece of the puzzle that did not fit—the strong broad optical emission lines in quasars versus the weak narrow emission lines in radio galaxies. This last major piece of the puzzle was solved when 3C234 and NGC 1068 were shown to have broad polarized emission lines, providing the first direct evidence of equatorial rings of dusty gas surrounding AGNs, which can obscure the broad-line region (Antonucci & Miller 1985).

2.2. Radio Jets

AGN jets exist on scales from solar system to galaxy separation scales, from $\lesssim$1 AU to $\gtrsim$1 Mpc, and are now observed on microarcsecond to degree scales using single dishes, long baseline arrays, and very long baseline arrays.

BL Lac objects (BLLs): low-power blazars that lack prominent broad emission lines

SPECIAL RELATIVISTIC EFFECTS

Superluminal Expansion

Suppose that radiation is emitted by a moving source S at time t_S from position $\mathbf{r}(t_S)$ along direction $\mathbf{n}$ to an observer O at large distance d, who receives it at a time $t_O = t_S - \mathbf{n}\cdot\mathbf{r}/c$ after the time that a pulse would have been received from the origin of the coordinate system. Ignoring cosmological expansion, the apparent speed of S observed by O is $v_{\rm apparent} = V\sin\theta/(1 - V\cos\theta/c)$, where $V = |\dot{\mathbf{r}}|$ and $\cos\theta = \mathbf{n}\cdot\dot{\mathbf{r}}/V$. This can be superluminal and has a maximum value ΓV, with the Lorentz factor $\Gamma = (1 - V^2/c^2)^{-1/2}$ when $V = c\cos\theta$. Typically $\Gamma \sim 10$. If S is a physical source (and this may not be the case), the Doppler factor associated with S is given by $\mathcal{D} \equiv \nu_O/\nu_S = T_{BO}/T_{BS} = [\Gamma(1 - V\cos\theta)]^{-1}$, where ν is the frequency and $T_B \equiv Sc^2/2k\nu^2\Omega$ is the brightness temperature for a source with flux density S subtending an angular size Ω.

Doppler Boosting

If the radiation has an intensity (flux $\mathrm{Hz}^{-1}\ \mathrm{sr}^{-1}$) I, then this transforms according to $I(\nu_O) = \mathcal{D}^3 I(\nu_S)$. The effect can be dramatic. The flux observed from an approaching, flat-spectrum ($\theta = \alpha = 0$), optically thin source with $\Gamma \sim 10$ is larger than that from an identical receding source by $\sim 6 \times 10^7$. The intensity is determined by solving the equation of radiative transfer in the galaxy frame transforming the emissivity from a frame moving with S to the O frame using $j(\nu_O) = \mathcal{D}^2 I(\nu_S)$. Likewise, the absorption coefficient transforms according to $\mu(\nu_O) = \mathcal{D}^{-1}\mu(\nu_S)$.

2.2.1. Three important jet scales. Reviews of the first three decades of very long baseline interferometry (VLBI) surveys and VLBI studies of parsec-scale jets are given by Wilkinson (1995) and Zensus (1997), respectively. More recently, Beasley (2002) led the Very Long Baseline Array (VLBA) Calibrator Survey, which has been augmented by a number of additional surveys, including observations of southern sources made with the Australian Long Baseline Array (Petrov 2011). Thus far, more than 12,000 AGNs have been observed by VLBI, and these form the basis of the Astrogeo Project (Petrov 2016). Other recent extensive VLBI studies of parsec-scale jets are those of 295 AGNs by the MOJAVE (Monitoring Of Jets in Active galactic nuclei with VLBA Experiments) group (Lister et al. 2016a) and the monthly 43-GHz VLBI observations of 34 γ-ray-bright blazars (Marscher et al. 2011, Jorstad & Marscher 2016).

AGN jets can be considered on three loosely defined scales. Most observations are of galaxy jets where the dynamical environment is dictated by the stellar/dark matter potential within the host galaxy and the interstellar medium (ISM). Black hole jets are the inward extension of galaxy jets to the gravitational radius of the black hole, $r_g \equiv GM/c^2$ (see the sidebar titled Black Holes). Here, the environment is dominated by the black hole potential and the inflow onto an accretion disk and the outflow from it (see the sidebars titled Black Hole Accretion and Classical and Revisionist Accretion Disk Theory). These two regimes straddle the radius of influence of the SMBH $R_{\rm inf} = GM/\sigma^2$, where σ is the 1D central stellar velocity dispersion and of order the Bondi (1952) radius, which is a measure of the distance at which the gravitational potential changes abruptly and from which gas can accrete onto the hole. Lobe jets are the outward extension of galaxy jets, from $\sim 0.1R_{\rm lobe}$ to $R_{\rm lobe}$, where $R_{\rm lobe}$ is the maximal extent of the jet or lobe. Here, the environment is controlled by the backflow from the end of the jet and the circumgalactic medium.

VLBI: very long baseline interferometry

2.2.2. Galaxy jets ($R_{\rm inf} \lesssim R \lesssim 0.1R_{\rm lobe}$). Jets are the conduits along which energy, momentum, mass, and magnetic flux flow from the black hole and its accretion disk to the giant radio lobes. Their original forms, their losses due to radiation, and their interactions with their surroundings determine what is observed.

BLACK HOLES

Einstein's general theory of relativity has been abundantly corroborated in the weak field limit, and its strong field, nonlinear version is consistent with many observations involving cosmology, gravitational radiation, and black holes (Meier 2012, Thorne & Blandford 2017). Black holes are now seen as inevitable consequences of stellar and galactic evolution. Massive black holes with masses $M \sim 10^{6-10}\,M_\odot$ appear to be present in the nuclei of most normal galaxies, including our own. Examination of a remarkable solution (Kerr 1963) for the metric of a spinning black hole shows that there is an event horizon with radius (measured by the circumference) $r_+ = r_g[1 + (1 - j^2)^{1/2}]$. The gravitational radius is $r_g \equiv GM/c^2 = 1.5(M/10^6\,M_\odot) \times 10^6$ km, and $\tau_g \equiv r_g/c = 5(M/10^6\,M_\odot)$ s is the gravitational time. $j \equiv \mathcal{J}c/(GM^2)$ is the dimensionless spin angular momentum of the hole with $|j| < 1$. The angular velocity of the hole is $\Omega_H = jc/2r_+$, with $|\Omega_H| < c/2r_g$. Many spin measurements are close to maximal (Reynolds 2014).

2.2.2.1. Structure and kinematics. Three key observational facts emerged in the early years of VLBI imaging: (*a*) they are one-sided jets (Wilkinson et al. 1977), (*b*) they have a compact flat-spectrum core at one end of a steep-spectrum jet (Readhead et al. 1978b), and (*c*) components are often seen to expand or to move along the jet away from the core at superluminal speeds (Gubbay et al. 1969, Zensus & Pearson 1987).

EHT: Event Horizon Telescope

By far the most comprehensive VLBI study monitoring blazars is that of the MOJAVE group (Lister et al. 2016a, Lister 2016b), where the results of VLBI monitoring observations of 400 AGN jets spanning 20 years are presented. Almost all objects observed have the same one-sided core-jet structure, as was seen in the earliest VLBI maps, and relativistic motion is usually observed with $v_{\rm apparent}$ ranging from $\sim 0.03c$ to $40c$. (In one object, PKS 0805-07, $v_{\rm apparent}$ reached $\sim 50c$ in 1996 before decelerating to $\sim 20c$.) Superluminal motion is common in FSRQs, BLLs, and narrow-line Seyfert 1 galaxies. Acceleration is observed in many superluminal components, and 32% of the jet features display nonradial motion while 4% show inward motion. Almost all the AGNs with the fastest moving components have been detected by the *Fermi Gamma-ray Space Telescope*, henceforth *Fermi*, indicating a strong correlation between bulk Lorentz factor and γ-ray emission. Within the first ~ 100 pc the majority of the features observed are superluminal and are accelerating.

Recent advances in millimeter VLBI have been reviewed by Boccardi et al. (2017), together with the roles of the global VLBI network and the present as well as the anticipated role of the Event Horizon Telescope (EHT). The 43-GHz VLBI observations of M87 (Mertens et al. 2016)

BLACK HOLE ACCRETION

AGN black holes are surrounded by orbiting gas. When this gas is able to cool on the inflow timescale, it will form a thin accretion disk in the equatorial plane with an inner radius $r > r_{\rm ISCO}$, the radius of the innermost stable circular orbit (ISCO), which shrinks from $9r_g$ to r_g as j increases from -1 to 1 (Meier 2012). The outer radius of the disk is unknown; self-gravitation, dust, and even stars can be important (Thompson et al. 2005). In this simple model, gas spirals inward under magnetic torques sustained by the magnetorotational instability (MRI) (Balbus & Hawley 1998) and plunges toward the event horizon within $r_{\rm ISCO}$.

However, the gas will not cool when the dimensionless accretion rate $\dot{m} \gtrsim 1$, where $\dot{m} \equiv \dot{M}/(4\pi GMm_p/\sigma_T c)$ is scaled to the Eddington rate, as the radiation is trapped by the inflowing gas and radiation pressure thickens the disk into a torus which can create a funnel which may be responsible for the initial collimation of radio quasar jets (Abramowicz & Fragile 2013). A torus supported by the pressure of hot ions may perform a similar function when the accretion rate is so low that electrons can remain mildly relativistic on a flow timescale (Yuan & Narayan 2014).

CLASSICAL AND REVISIONIST ACCRETION DISK THEORY

Initially, interiors of black hole accretion disks were modeled like those of stars. At very low $\dot{m}$ the disk was thought to be a geometrically thin, optically thick hot ionized plasma supported by gas pressure and the opacity given by free-free absorption, similar to low-mass stars (Shakura & Sunyaev 1973). Such disk inflow is called outer region inflow. For higher rates, in the range $10^{-3} \sim \dot{m}_{\rm M} \lesssim \dot{m} \lesssim \dot{m}_{\rm I} \sim 0.2\, m^{-1/8}$, middle region inflow occurs, with the opacity near the black hole dominated by Thomson electron scattering, and the gas pressure still dominant. For even higher rates, in the range $\dot{m}_{\rm I} \lesssim \dot{m} \lesssim 1$, radiation pressure dominates the inner region inflow. In the early scaling models, inner region flow was found to be secularly and thermally unstable, but numerical simulations of the process are still inconclusive. For $\dot{m} \gtrsim 1$, radiation pressure should drive a strong outflowing wind.

However, at low accretion rates ($\dot{m} \lesssim \dot{m}_{\rm A} \sim 0.05$–$0.1$) black hole accretion may be more like a geometrically thick, optically thin stellar corona described by a very hot, two-temperature advection-dominated accretion flow (ADAF) with ions at $\sim 10^{12}$ K supplying the pressure and electrons at $\sim 10^{9-11}$ K producing most of the emitting radiation. Note that, at accretion rates below $\dot{m}_{\rm A}$, outer region inflow simply does not exist as $\dot{m}_{\rm A} > \dot{m}_{\rm M}$ is always the case. Similarly, even middle region inflow should not exist for massive black holes ($m > 10^{3-5}$), as $\dot{m}_{\rm A} > \dot{m}_{\rm I}$ because of the mass dependence of $\dot{m}_{\rm I}$. So AGNs might be expected to have only three types of accretion flow: ADAF at low rates, unstable inner region flow at high rates, and outflow at super-Eddington rates. An alternative view (Blandford & Begelman 1999) of low-rate accretion is that the torque always does so much work on the outer disk that it is unavoidably unbound and once the inflow is unable to radiate the binding energy released, there will be an outflow so that the mass flow into the black hole is much less than the mass supply rate at large radius. In this case the flow is more accurately described as an ejection disk. If the inflow is strongly magnetized, the disk may remain thin at all radii (Königl & Kartje 1994).

show clearly a mildly relativistic velocity component along the sheath and a faster component $\Gamma = 2.5$ along the spine. The global millimeter VLBI network has also been used at 86 GHz to study the jet of M87 down to $\sim 7\, r_{\rm g}$ (Kim et al. 2018) and shows limb brightening, and hence evidence of a spine-sheath structure down to this scale, which therefore appears to be anchored to the inner portion of the accretion disk. The result of stacked images from this study is shown in **Figure 1**.

The very high-resolution 22-GHz observations of 3C84 made with the global VLBI network and RadioAstron space VLBI mission (Giovannini et al. 2018 and **Figure 2**) show an edge-brightened jet down to within 30 μas from the core, and they conclude that the jet either goes through a very rapid lateral expansion on scales $\lesssim 100\, r_{\rm g}$ or is launched from the accretion disk. The global millimeter VLBI network has been used at 86 GHz to study the polarization of 3C84 by Kim et al. (2019), who find that the polarization is consistent with an underlying limb-brightened structure, and they find, due to its uniform rotation measure (RM) structure, that the Faraday depolarization is most likely due to an external screen.

2.2.2.2. Polarization. A very intensive linear polarization study was carried out on 484 AGNs using observations from the MOJAVE program as well as from the VLBA archive, covering 20 years from 1996–2016 (Pushkarev et al. 2017). All told, 5,410 VLBA observations were used in this study. The principal results are: (*a*) For all classes, fractional polarization increased with core separation; (*b*) there was a clear increase of polarization fraction toward the edge of the jet, interpreted as being due to the fact that the greater depth of the jet along lines of sight closer to the axis of the jet, compared with the edge of the jet, leads to more Faraday depolarization; (*c*) 40% of jet cores have a preferred electric vector position angle (EVPA) direction from epoch to epoch; (*d*) BLL cores have more stable EVPAs than quasars and tend to be aligned with the

RM: rotation measure

EVPA: electric vector position angle

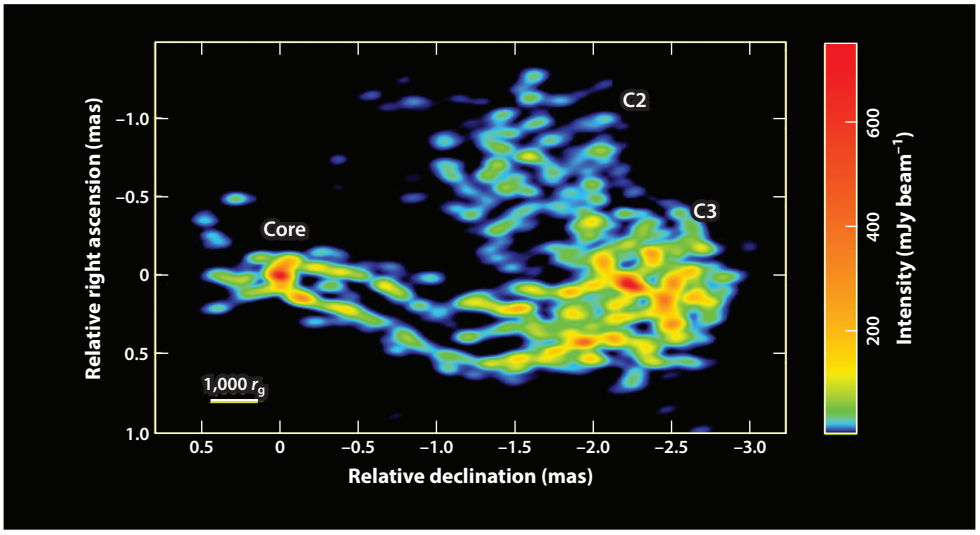

Figure 2

22-GHz image of the black hole jet in 3C84 made with the global VLBI network and RadioAstron space VLBI antenna (Giovannini et al. 2018). With a viewing angle of $\sim 18^\circ$, the deprojected distance from core down to component C3 is $\sim 10^{4.5}\, r_g$ or ~ 3 pc. Rather than collimating in a semiparabolic fashion, like M87, the black hole jet in 3C84 appears to have a nearly uniform width from near the core region to a distance of $\sim 10^4 r_g$. Abbreviation: VLBI, very long baseline interferometry.

initial jet direction; (*e*) BLL jets show the same tendency; and (*f*) quasars and radio galaxies show no such tendency.

A review of the full Stokes imaging results, i.e., including circular polarization, from the MOJAVE program is given by Homan et al. (2018), presenting multi-epoch results from 2002 to 2009, for 278 objects over 6 epochs on average. Typical levels of circular polarization, when detected, range from 0.3% to 0.7%, with the maximum observed being 1% in NRAO 140, which was also fairly stable, unlike most sources. The maximum circular polarization is always seen in the core component, and the large majority showed a preferred sign, which persisted for 3.5 years—i.e., longer than the duration of a typical flare. 3C279 has been observed for more than 20 epochs spanning 14 years, all with the same sign of circular polarization.

Faraday RM studies, reviewed by Gabuzda et al. (2017), have been pursued intensively by a number of groups. Zavala & Taylor (2004) made a systematic study of the RM in 40 quasars, radio galaxies, and BLLs, and found that the RMs in both quasars and BLLs are very similar in both the cores (typically 500 to several thousand rad m^{-2}) and the jets (typically 500 rad m^{-2} or less). In contrast, the cores of radio galaxies are generally unpolarized, whereas the jets exhibit RMs ranging from a few hundred to $\sim 10^4$ rad m^{-2}. Their results can best be explained in terms of a screen in close proximity to the jet, which could very well indicate the presence of a sheath around the jet. Magnetic fields ~ 1 μG are deduced in the screen.

The MOJAVE group has carried out a systematic study of Faraday rotation in 191 extragalactic radio jets, using multifrequency VLBA observations over 12 epochs, and found that quasars have on average larger RMs than do BLLs. Of particular interest is the fact that they observed transverse gradients in RM (Hovatta et al. 2012) in four blazars including 3C273, in which the RM changes sign over the transverse cuts, which they interpret as evidence for a helical magnetic field. This result has been confirmed (Wardle 2018) and provides firm evidence of a toroidal magnetic field component, which requires a current down the jet of 10^{17}–10^{18} A.

ACZ: acceleration and collimation zone

A very interesting discovery in optical polarization observations of AGNs is that large rapid rotations of the EVPA of some AGNs are correlated with γ-ray flares (Marscher et al. 2008). While an intrinsic connection between rotations and γ-ray flares is difficult to establish on an event-by-event basis, due to uncertainties on both the γ-ray and polarimetry sides, a more general connection between optical polarization and γ-ray activity has now been firmly established by the RoboPol program (Blinov et al. 2018).

2.2.3. Black hole jets ($r_g \lesssim R \lesssim R_{inf}$). Most VLBI imaging is on scales larger than or of order R_{inf}. Our understanding of black hole jets derives from a few well-studied examples.

2.2.3.1. M87 imaging. Most images we have of black hole jets are associated with lower-power Fanaroff–Riley type 1 (FR-I) objects—M87, BL Lac, and 3C84. Because of the proximity of M87 (17 Mpc), VLBI imaging of its jet affords a very detailed look at what lies inside the core region ($R < 10^6\, r_g$). This includes the acceleration and collimation zone (ACZ). The most detailed and systematic VLBI study of the innermost M87 jet carried out so far is that of Walker et al. (2018), which is based on 50 VLBA 43-GHz observations with a resolution of $\sim 60 \times 120\, r_g$, taken over 17 years. These observations show the following (**Figure 1**):

- an asymmetric jet and counter-jet are found in the inner 1.5 mas (0.12 pc);
- both jet and counter-jet are edge brightened;
- both jet and counter-jet show an initial rapid widening, followed by a narrowing and then a second widening, at which point the counter-jet becomes invisible;
- the jet is subsequently collimated;
- proper motions and the intensity ratios of the jet and counter-jet indicate acceleration from $v_{apparent} < 0.5c$ to $v_{apparent} > 2c$; and
- polarization observations suggest a helical magnetic field close to the core.

The high-frequency, high-resolution VLBI observations of M87 show the jet accelerating smoothly, with a parabolic profile, to relativistic speed over a deprojected radius ~ 300 pc $\sim R_{inf}$ (Nakamura & Asada 2013, Walker et al. 2018). At this point a strong, quasi-stationary shock, HST-1, appears to form in the flow (**Figure 1**) and regularly ejects superluminal components (Cheung et al. 2007, Nakamura et al. 2010) at apparent speeds up to $6c$ (Biretta et al. 1999, Giroletti et al. 2012) before the jet slows and widens (**Figure 3**). The helical structure observed beyond HST-1 suggests that the magnetic field is still dynamically strong here (Asada & Nakamura 2012). A similar, stationary transition is observed near the component C7 in BL Lac. This is also at a deprojected radius $\sim R_{inf}$ and also creates superluminal components.

The new EHT study of the core of M87 at 230 GHz (Akiyama et al. 2019) (with an effective FWHM beam of 20 μas; see **Figure 1**) reveals a ring of diameter ∼45 μas, equivalent to 12 r_g for a black hole mass of $6.5 \times 10^9\, M_\odot$. The peak brightness temperature is $\sim 6 \times 10^9$ K, at least ten times the brightness of the center of the ring. The azimuthal variation is consistent with Doppler brightening from relativistic electrons orbiting on circular orbits with angular velocity at an angle $\sim 163^\circ$ to the observer direction (Walker et al. 2018). This image provides strong prima facie evidence that the M87 jet is formed very close to a massive black hole.

2.2.3.2. 3C84 imaging. Recent observations of 3C84 tell a somewhat different story (Hodgson et al. 2018). The jet appears to expand to create a strongly edge-brightened cylinder with a diameter $\sim 1,000\, r_g$, increasing slowly with height, out to a deprojected distance $\sim 3 \times 10^4\, r_g$, well within R_{inf}. The jet appears to be propagating through and interacting with a constant pressure cocoon, either a very hot gas or, more plausibly, a magnetized sheath.

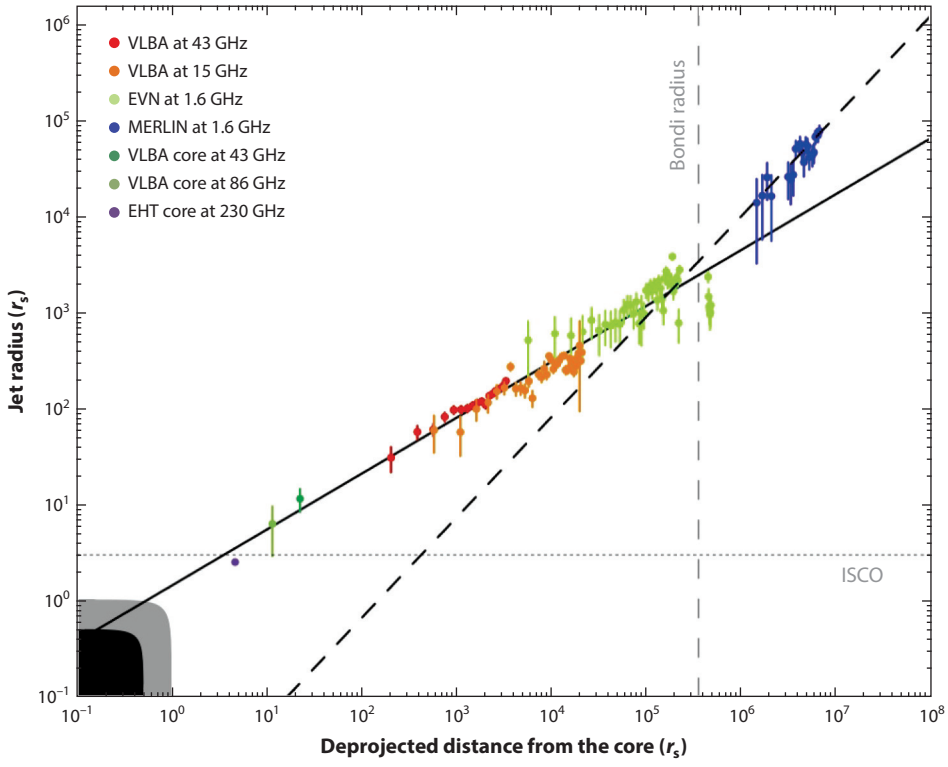

Figure 3

Transverse radius versus R for the black hole and galaxy jets in M87 (see **Figure 1*c*,*d***). The jet collimates (and accelerates) in a semiparabolic fashion steadily from the black hole to a maximum apparent velocity of $\sim 6c$ at a prominent optical feature known as HST-1 ($10^6 r_g \sim R_{inf}$), where there is a change in slope or jet collimation break. Beyond that the jet flares in a linear fashion and decelerates to subrelativistic speeds (Asada & Nakamura 2012). The Bondi radius is about 1.2 R_{inf} here. Figure adapted from Nakamura & Asada (2013) and reproduced by permission of the AAS. Abbreviations: EHT, Event Horizon Telescope; EVN, European VLBI Network; ISCO, innermost stable circular orbit; MERLIN, Multi-Element Radio-Linked Interferometer Network; VLBA, Very Long Baseline Array.

2.2.3.3. BL Lac imaging. Very high-resolution VLBI imaging of BL Lac indicates that the structure of the unresolved VLBI core is actually very rich and complex. MOJAVE observations of BL Lac (Cohen et al. 2014) show that a stationary component (C7, probably a stationary shock) lies 0.26 mas from the true core (where the black hole is believed to reside) or ~3 pc deprojected, assuming a BL Lac viewing angle of $\sim 6^\circ$. The stationary component appears to be the source of the ejected superluminally moving components seen in BL Lac outbursts. Furthermore, Cohen et al. (2015) find that, in addition to these moving components (identified as longitudinal fast waves or shocks in the jet's helical magnetic field moving at a speed $\beta_F \sim 0.68$ in the rest frame of the $\Gamma \sim 4.5$ jet), there are transverse Alfvén waves traveling downstream at a slower velocity ($\beta_T \sim 0.25$). These results, along with the generally observed longitudinal EVPA in BLLs (Gabuzda et al. 2004), are further evidence that these jets are dominated by a strong helical magnetic field even downstream of the C7 shock.

2.2.3.4. Jet collimation. In M87, unlike BL Lac, the HST-1 region has not been examined for long-term traveling transverse Alfvén waves, but there was a transverse shift in the position angle

FR class:
Fanaroff–Riley class

of the HST-1 ejecta from -65° to -100° over the period 2007.00–2011.65. Interestingly, if the $\sim 10^{9.8}$ $M_\odot$ M87 black hole system (Walsh et al. 2013) is simply scaled linearly down to the size of the $\sim 10^{7.5}$-$M_\odot$ BL Lac (Titarchuk & Seifina 2017), the distance between HST-1 and the M87 black hole shrinks from ~ 300 pc to ~ 3 pc, similar to the distance between C7 and the BL Lac black hole.

Studies of the M87 jet width upstream and downstream of HST-1 have revealed important clues to jet acceleration, collimation, and propagation (Nakamura & Asada 2013). Downstream of HST-1 (the analog of the jet in traditional VLBI core-jet sources) the flow has a fixed conical opening angle. This result justifies the assumption of a relativistic conical flow in theoretical work on VLBI jets (Blandford & Königl 1979). Upstream of HST-1, however, the jet shape is semi-parabolic, with a profile of radius $r \propto$ SMBH distance $R^{0.58\pm0.02}$, which requires a modification of this model (Algaba et al. 2017). Astonishingly, even higher-resolution observations with the VLBA up to 86 GHz and with EHT at 230 GHz (Doeleman et al. 2012) already show that this profile persists all the way down to $R \sim 6r_g$ above the black hole.

2.2.3.5. Polarization and acceleration. Detailed studies of the linear polarization in M87 at radio and optical wavelengths have been carried out with the VLA and *Hubble Space Telescope* (HST), as described by Avachat et al. (2015). The most striking findings are that (*a*) both images show similar polarization structure near the nucleus, (*b*) with the magnetic vectors parallel to the jet axis, and (*c*) at the knot HST-1, the degree of polarization is significantly greater in the optical images and the magnetic vectors are perpendicular to the jet axis. This is interpreted as showing that the higher-energy emission along the jet comes from deeper within the jet and that the shock at HST-1 is deeply embedded in the jet.

Finally, proper motion studies of the M87 jet (Asada et al. 2014) show that acceleration is steady from an apparent speed of $\sim 0.01c$ at a black hole distance of $\sim 400\, r_g$ to a superluminal peak of $\sim 6c$ at HST-1 ($\sim 5 \times 10^5\, r_g$), and then deceleration occurs to $\sim 0.4\, c$ at $2 \times 10^7\, r_g$ from the black hole.

To summarize, in low-luminosity FR-I sources, jet acceleration and collimation to superluminal speeds appears to occur often, within the traditional, unresolved VLBI core over a distance of $r_\infty \sim 10^{5-6} r_g$. This ACZ terminates in a strong shock, which then ejects the multiple superluminal jet events that have been seen in VLBI observations since the early 1980s. The high speed of relativistic jets, therefore, does not develop within a short distance from the black hole, but rather is produced slowly over a distance of hundreds of thousands of black hole radii as the jet propagates out of the galactic center.

2.2.4. Lobe jets ($0.1R_{\rm lobe} \lesssim R < R_{\rm lobe}$). Jets inflate large radio-emitting lobes and bubbles, and their observed properties just before they end provide strong clues to how they have developed.

2.2.4.1. Fanaroff–Riley (FR) class. Radio maps of AGNs made with the Cambridge One-Mile Telescope showed that many radio sources are double-lobed like Cygnus A (see **Figure 4**) and that they have fairly compact regions, or hot spots, in their lobes as well as the compact cores in their nuclei. This supported continuous energy supply from the nucleus to lobes by jets (Hargrave & Ryle 1974). A major advance in classification was the division of double radio sources into lower-radio-luminosity FR-I sources, in which the highest-brightness regions are closer to the nucleus than the low-brightness extremities, and higher-radio-luminosity FR-II sources when they are not (Fanaroff & Riley 1974).

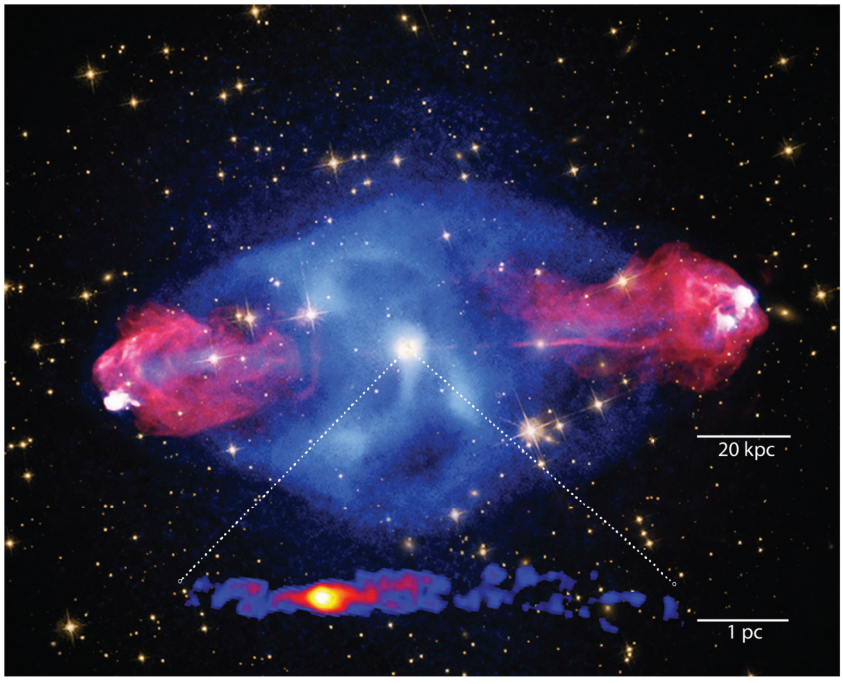

Figure 4

Comparison of radio (*red*), X-ray (*blue*), and optical images of the Cygnus A FR-II radio galaxy (*center*). While the X-ray traces primarily hot old cocoon emission and the radio traces the jet and new cocoon emission, the three primary hot spots are bright in both energy bands with a synchrotron peak in the radio and a Compton scattering peak in the X-ray. The nearly symmetric black hole jet is shown in an inset at bottom, with a scale 20,000 times smaller than the larger image. Images adapted with permission from the following: X-ray, NASA/CXC/SAO; optical, NASA/STScI; radio, NSF/NRAO/AUI/VLA; VLBI inset, Boccardi et al. (2017). Abbreviations: AUI, Associated Universities Incorporated; CXC, Chandra X-Ray Center; FR-II, Fanaroff–Riley type 2; SAO, Smithsonian Astrophysical Observatory; STScI, Space Telescope Science Institute; VLA, Very Large Array; VLBI, very long baseline interferometry.

2.2.4.2. FR-II jets. FR-II jets are often quite asymmetric, and the brighter one is accompanied by lower Faraday rotation verifying that it is approaching and is still Doppler-beamed (Garrington et al. 1988). So, FR-II jets appear to emerge from their galactic nuclei with at least mildly relativistic speed and a significant fraction of their initial power. The first FR-II jet was discovered in 3C219 (Turland 1975), and this was soon followed by a spectacular 200-kpc-long jet in NGC 6251 (Waggett et al. 1977).

2.2.4.3. FR-I jets. Much has been learned from a systematic VLA polarimetric survey of ten FR-I jets by Laing & Bridle (2014). It was concluded that they expand faster than linearly within 1–30 kpc—after which they expand linearly. Meanwhile, the magnetic field transitions from axial to toroidal. A slower jet boundary later is observed, and a velocity gradient can be inferred across the jet. Spectral data, including X-ray observations, imply that particles are being continuously accelerated in the jet.

CSO: compact symmetric object

2.2.4.4. Compact symmetric object jets. Compact symmetric objects (CSOs) (Wilkinson et al. 1994) are very likely young FR-II objects (Readhead et al. 1996). These have been shown to

SED: spectral energy distribution

indeed be young and to have ages in the range 20–2,000 years (Gugliucci et al. 2005). The first large uniform sample of CSOs to be studied is that of Tremblay et al. (2016), who show that the CSO class exhibits both FR-I and FR-II morphology, and, furthermore, the morphology appears to depend on luminosity, with the transition occurring at the same luminosity as in their larger cousins.

2.3. γ-Ray Observations to Very High Energies

The launch of *Fermi* in 2008 and its highly successful operation over the past decade has had a tremendous impact on studies of blazars. *Fermi* surveys the whole sky every 3 hours over the energy range 20 MeV–300 GeV. There have been corresponding advances in ground-based atmospheric- and water-Cerenkov telescopes, including the High Altitude Water Cherenkov Observatory, High Energy Stereoscopic System, Major Atmospheric Gamma-ray Imaging Cherenkov (MAGIC), and Very Energetic Radiation Imaging Telescope Array System (VERITAS), that have extended the spectral range to energies beyond ∼10 TeV (and can have sensitivity to ∼100 TeV) in some AGNs (Funk 2015, Gonzalez 2015, Lauer 2015, Lindfors 2015, Lott et al. 2015). γ-ray observations complement radio studies with an extensive—up to 20 octave—spectral energy distribution (SED) and rapid variability. These remarkable advances in γ-ray capability have spearheaded a large global program of multiwavelength and multimessenger observations.

In a radio flux density–limited sample of flat-spectrum AGNs selected at 5 GHz, it was found that only ∼20% of the objects are detected in γ-rays (Karouzos et al. 2011). However, all of the *Fermi*-detected blazars north of declination −20° are detected in the Caltech Owens Valley Radio Observatory (OVRO) 40-m telescope monitoring campaign (Richards et al. 2011). Karouzos et al. (2011) find no strong link between fast apparent speeds and γ-ray detectability, as measured with *Fermi*. They argue that this is evidence for a spine-sheath structure (Sol et al. 1989, Laing 1996), in which the outer layers of the relativistic jet, which form the sheath, have slower bulk velocity along the jet axis than do the inner layers, which form the spine. Such a structure could also explain the relative fractions of AGNs that are γ-ray bright and radio bright, if the spine is predominantly γ-ray-emitting and the sheath is predominantly radio-emitting.

In a comprehensive review of γ-ray observations of AGNs, Madejski & Sikora (2016) found that the γ-ray flux density variations in blazars show generally greater fractional amplitudes than the other observed bands, and stronger flares tend to occur when the flux density is at a higher-than-average level, with the activity lasting anywhere from several days to several months. It is useful to consider two subclasses of AGNs based on the blazar sequence of Fossati et al. (1998), Ghisellini et al. (1998), and Ghisellini (2016): (*a*) the high-synchrotron-peaked BLL (HBL) and low-luminosity, line-less BLL and (*b*) the powerful FSRQs, which have high luminosities and strong emission lines (see also **Tables 1** and **2** and **Figure 5**). The FSRQ-type blazars show greater amplitude of γ-ray variability than the HBL-type blazars, but HBL blazars show the greatest

Table 1 Classification of radio-loud AGNs by their radio properties

Abbreviation	Expansion	Definition	Density (L_{bol})[a]
FR-I	Fanaroff–Riley type 1	Low-power, edge-darkened radio source	$\sim 10^{4}$ ($<10^{42}$)
FR-II	Fanaroff–Riley type 2	High-power, edge-brightened radio source	$\sim 10^{1.5}$ ($>10^{42}$)
BLL	BL Lac object	Compact radio source with polarized optical continuum and weak or no emission lines	$\sim 10^{2.3}$ ($<10^{42}$)
FSRQ	Flat-spectrum radio quasar	Compact radio source identified with a quasar	$\sim 10^{0.8}$ ($>10^{42}$)

[a]Density is local and in units of Gpc^{-3}; AGN L_{bol} is in erg s^{-1} (Braun 2012, Ajello et al. 2014, Tadhunter 2016).

Table 2 The blazar sequence

Abbreviation	Expansion	Probable radio parent	Emission lines
Extreme HBL	TeV blazars (BLL)	Low-luminosity FR-Is	Weak
HBL	High-energy peaked (blue) BLL	FR-I sources	Weak
IBL	Intermediate-energy peaked BLL	FR-I/II break sources	Weak
LBL	Low-energy peaked (red) BLL	Class B FR-IIs	Weak
FSRQ	Flat-spectrum radio quasar	BLRG, FR-II QSR	Strong

Abbreviations: BLL, BL Lac object; BLRG, broad-line radio galaxy; FR, Fanaroff–Riley; QSR, quasi-stellar radio source.

variability amplitude in the very high-energy (VHE) γ-rays. Furthermore, the FSRQs have soft γ-ray spectra, while the HBL blazars have hard γ-ray spectra. Madejski & Sikora (2016) conclude that the broadband data strongly suggest that the primary dissipation of the jet energy converted to blazar power at γ-ray energies occurs beyond $\sim 10^4 r_g$ and that the size of the dissipation region, as inferred from the γ-ray variability timescale, is very small.

A corresponding review of VHE observations of AGNs (Prandini 2017) shows that 70 AGNs have been detected, including 3C279 ($z = 0.54$), PKS 1441+25 ($z = 0.94$), and S3 0218+35 ($z = 0.95$). The highlights are as follows: (*a*) most of the TeV AGNs are HBLs; (*b*) the only extragalactic non-AGN sources are the nearby starburst galaxies M82 and NGC 253; (*c*) the large majority of sources are at $z < 0.5$ and all are at $z < 1$; (*d*) a number of detected objects have no redshift measurement, as is not atypical of BLLs; (*e*) although FSRQs form the majority of

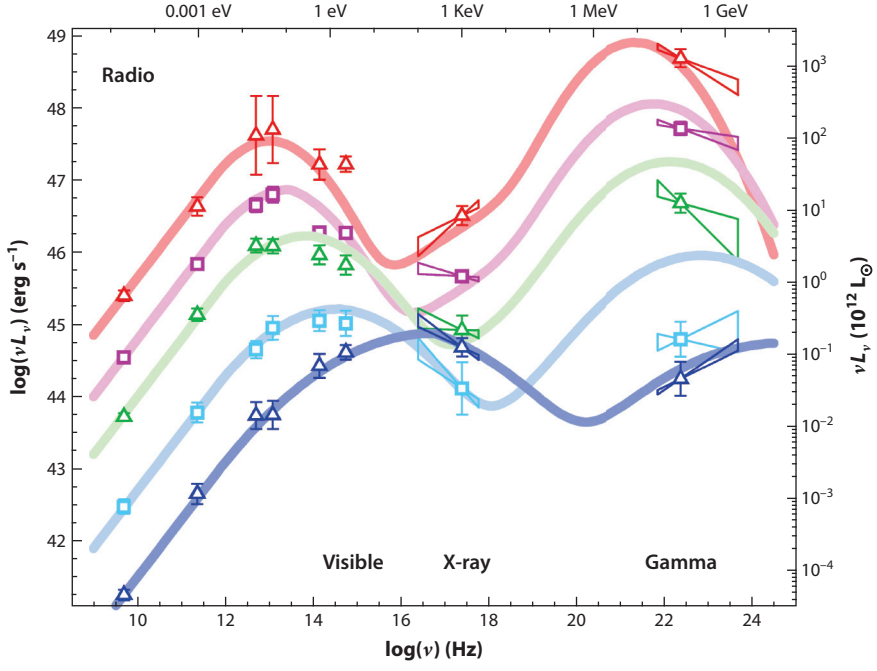

Figure 5

The blazar sequence (**Table 2**) in the electromagnetic spectrum, showing a high-powered flat-spectrum radio quasar (*red*), LBL (*pink*), medium-luminosity IBL (*green*), HBL (*light blue*), and low-powered extreme HBL/TeV (*dark blue*) blazar, after Fossati et al. (1998). Abbreviations: BLL, BL Lac object; HBL, high-energy peaked blue BLL; IBL, intermediate-energy peaked BLL; LBL, low-energy peaked BLL.

AGNs detected by *Fermi*, they make up only a small fraction of the TeV-detected sources, as might be expected from the blazar sequence; (*f*) seven FSRQs have been detected at the highest energies, with two of them being the highest redshift AGNs detected at VHE thus far, and one of them being the gravitationally lensed system B0218+357; and (*g*) the high-redshift systems place important constraints on our estimates of the extragalactic background light.

2.4. Optical, IR, UV, and X-Ray Observations

HST, *Chandra*, and the *Nuclear Spectroscopic Telescope* (NuSTAR), especially, have also transformed our understanding of jets by connecting the radio to the γ-ray emission and helping us understand where particles are accelerated along jets and to what energies. X-rays in AGNs originate from the AGN accretion disk itself, as well as from the jet. The general properties are reviewed by Brandt & Alexander (2015), and a detailed discussion of the X-ray variability in 81 AGNs observed with NuSTAR is given by Rani et al. (2017). 65% of their sources show significant variability on hourly timescales. There are several comprehensive reviews of X-ray observations of relativistic jets (Harris & Krawczynski 2006, Sambruna & Harris 2012, Schwartz et al. 2015). A key discovery of *Chandra* has been that of the emission from almost 100 relativistic jets, some of which extend up to hundreds of kiloparsecs (see, e.g., **https://hea-www.harvard.edu/XJET/**). The X-ray jets detected by *Chandra* are dominated by bright knots of emission. In the powerful objects, they also terminate in hot spots (**Figure 4**). It has been found that powerful FR-II jets are 100 times too bright to be radiating by synchrotron self-Compton emission. The possibility that the electrons are scattering cosmic microwave background (CMB) photons has been suggested, but this requires high bulk Lorentz factors and angles close to the line of sight. A comprehensive discussion of this problem and its possible solutions is given by Georganopoulos et al. (2016).

A prime example is that of the jet in 3C111, which Clautice et al. (2016) have studied with both *Chandra* and HST. As is typical in these cases, the jet is seen in X-rays through knots that coincide with radio knots and in the hot spots in which the jets terminate. Moreover, in the case of two of the brightest compact regions, where the X-ray and radio observations have sufficient resolution, these do not coincide precisely, but the peak of the X-ray feature is upstream of the peak of the radio feature, thereby providing clear evidence of two populations of relativistic electrons in different locations. This observation plus the implied velocity of the approaching hot spot strongly rule out external Compton scattering of CMB photons (EC/CMB) models and favor a two-component synchrotron model, thereby providing strong evidence for the multi-zone model.

The jet in M87 has been studied intensively with *Chandra* (Marshall et al. 2002). Almost all the optically bright knots are seen in X-rays, with the core being the brightest feature. Synchrotron models fit the knots in the jet well.

The combined X-ray results from *Chandra*, *Suzaku*, and *Swift* observations of 3C273 (Madsen et al. 2015), and especially the high-energy NuSTAR, multi-epoch *International Gamma-Ray Astrophysics Laboratory*, and *Fermi* observations, make it possible to separate out the coronal emission plus disk reflection component from the jet component. They show that the jet component can be fitted by a log-parabola model that peaks at $\sim$2 MeV.

An example of the results of a well-coordinated multiband campaign to determine the SED of an AGN (in this case Mkn421), combining observations from GASP-WEBT (the GLAST-AGILE Support Program of the Whole Earth Blazar Telescope), *Swift*, NuSTAR, *Fermi*, MAGIC, VERITAS, and other instruments, is shown in **Figure 6**, which is adapted from Balokovic et al. (2016). The Bactrian shape of the SED is typical of AGNs, and it is by now well established that the lower-frequency peak is due to synchrotron emission. Although the higher-frequency peak is widely believed to be due to inverse Compton scattering, as we have seen above, it is possible that

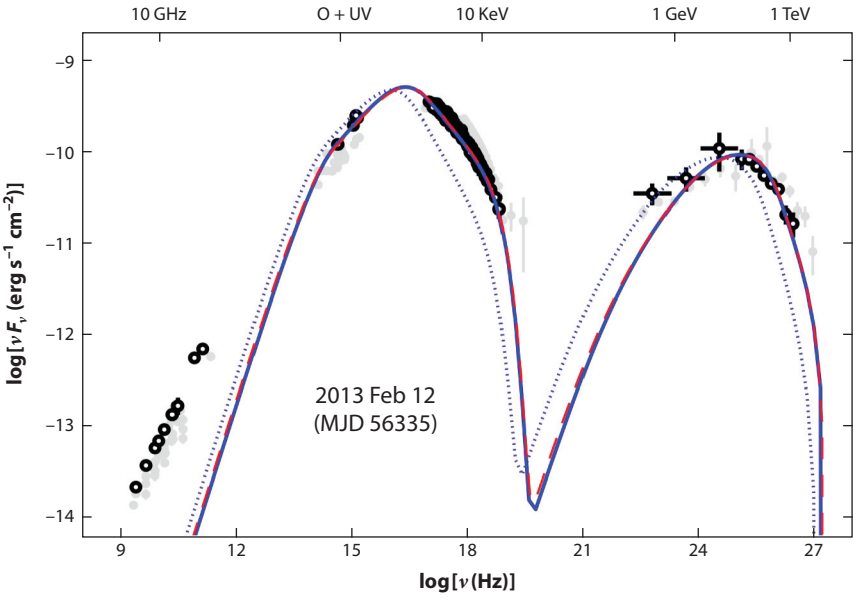

Figure 6

Spectral energy distribution of Mkn421 combining observations from GASP-WEBT, *Swift*, NuSTAR, *Fermi*, MAGIC, VERITAS, and other instruments (Balokovic et al. 2016). The solid blue line assumes a simple one-zone SSC model, which these authors argue against based on the fact that the synchrotron cooling time is a factor of 30 shorter that the variability timescale. The gray symbols in the background are from Abdo et al. (2011). Abbreviations: AGILE, *Astro-rivelatore Gamma a Immagini Leggero*; GASP-WEBT, GLAST-AGILE Support Program of the Whole Earth Blazar Telescope; GLAST, *Gamma-ray Large Area Space Telescope*; MAGIC, Major Atmospheric Gamma-ray Imaging Cherenkov; NuSTAR, *Nuclear Spectroscopic Telescope*; SSC, synchrotron self-Compton; VERITAS, Very Energetic Radiation Imaging Telescope Array System.

it too might, at least in some cases, be due to synchrotron emission. Observations of an individual γ-radio flare in M87 support the view that the γ-rays originate within $\sim 100\, r_g$ (Hada et al. 2014).

Many SED studies of AGNs use the one-zone model, which assumes that the emission causing both the synchrotron peak and the inverse-Compton peak originates from the same particle population. This assumption has been challenged in view of the degree of complexity seen in the radio emission regions, which probably persists down to the smallest scales in these extremely energetic objects. In the case of Mkn421, Balokovic et al. (2016) show that the synchrotron cooling timescale ~1,000 s, whereas $\tau_{var} \approx 9$ h, showing that it is unlikely that the emission is dominated by a single, shocked region. This argues for a multizone model.

2.5. Ultrahigh-Energy Cosmic Rays and Very High-Energy Neutrinos

Relativistic jets associated with SMBHs are plausible sites for the production of both high-energy (PeV-EeV) and ultrahigh-energy cosmic rays (~1–200 EeV) (Matthews 2018). This is because the potential difference across an electromagnetic jet powered by a spinning black hole and carrying a power $L_{jet} \sim 10^{45}$ erg s^{-1} is ~100 EV (see the sidebar titled Electromagnetic Effects). [It is unknown how much of this potential is actually available for particle acceleration, but it is worth noting that the Crab pulsar, which has a rotational electromotive force (EMF) of ~50 PV, manages to accelerate electrons in the nebula to at least ~3 PeV.] Recent analysis of Auger composition data (Bellido et al. 2018) are consistent with a maximum rigidity of ~1–4 EVc^{-1}, which only

ELECTROMAGNETIC EFFECTS

Traditional models of accretion disks conserve mass and angular momentum. Energy is transported radially outward, and the inevitable energy dissipation is supposed to be balanced by radiative loss from the disk surfaces. However, in the absence of radiative loss, a magnetohydrodynamic (MHD) wind can remove angular momentum and energy in the same ratio as they are released by the inflowing matter, obviating the need for dissipation (Blandford 1976, Lovelace 1976, Blandford & Payne 1982). The power and mass loss in the wind depend upon subtle physics, just as is the case with the solar wind. If there is open magnetic flux $\Phi_{\rm disk}$ threading a portion of the disk orbiting with angular velocity $\Omega_{\rm disk}$, then the wind power may be estimated (in S.I. units) by $L_{\rm disk} \sim \Phi^2_{\rm disk}\Omega^2_{\rm disk}/\mu_0 V_{\rm A\,crit}$, where $V_{\rm A\,crit}$ is the Alfvén speed at the critical point.

In addition, a portion $[1-(r_+/2r_{\rm g})^{1/2}]Mc^2$ of the mass of the hole is associated with its spin (Penrose 1969) and is extractable by electromagnetic stress (Blandford & Znajek 1977, McKinney & Narayan 2007, Penna et al. 2013). The power extracted can be calculated by solving the Einstein–Maxwell equations assuming an external current distribution and regularity at the horizon. The induced EMF is $V \sim \Omega_{\rm H}\Phi_{\rm H}/2$, where $\Phi_{\rm H}$ is the magnetic flux threading the horizon. The effective resistances associated with the horizon and a relativistic outflow are both $\sim$ 50 Ohm, and so the jet power and current are $L_{\rm jet} \sim 10^{45}(V/100\,{\rm EV})^2\,{\rm erg\,s^{-1}}$ and $I \sim (V/100\,{\rm EV})\,{\rm EA}$, respectively. This hole will gain mass at a rate $\sim 5\times10^7\,(L_{\rm jet}/10^{45}\,{\rm erg\,s^{-1}})\,{\rm M_\odot\,Gyr^{-1}}$ while losing spin energy at twice this rate.

requires a jet power $>3\times10^{44}\,{\rm erg\,s^{-1}}$. Furthermore, the recently discovered dipole anisotropy, when combined with a Galactic magnetic field model, suggests that M87/the Virgo cluster is a discrete source (Globus et al. 2019). There are only a few other sites where the highest-energy particles could be created (Hillas 1984; see also Section 4.1.1). A concern with this proposal is that, although high-energy hadrons may be accelerated in AGN jets, they may also be subject to catastrophic losses (Section 4.2.2.6).

Neutrinos with energies in the TeV to a few PeV range have been detected and associated with AGN jets. Recently, the possible identification of a single neutrino emitted with an energy $\sim$400 TeV with a flaring blazar, TXS 0506+056, has been reported (IceCube Collab. 2018). However, the lack of a correlation of the arrival directions of other neutrinos with known blazars suggests that no more than a quarter of these neutrinos derive from *Fermi* blazars (Aartsen et al. 2017).

2.6. Variability: Relative Locations of the Multiband Emission Regions

A key question in AGN studies is that of the relative locations of the emission regions in different bands. The earliest VLBI images showed a clear pattern in which the emission from higher frequencies occurs closer to the central engine (Readhead et al. 1978b). Given the one-sided jet morphology (Wilkinson et al. 1977), it was immediately clear that higher-frequency observations were penetrating the optically thick, flat-spectrum core at the end of the jet and probing deeper into the jet toward the SMBH. This pattern has now been found to be the case in most blazars observed with VLBI. In general, therefore, at radio frequencies, the higher-frequency emission is located closer to the SMBH than the lower-frequency emission. The interesting question here is whether the same is true when going to even higher-energy bands, including γ-rays. Since only VLBI offers mas resolution, for the most part the study of the relative locations of the emission regions in different observing bands has depended on variability and SED studies.

There have been many radio monitoring surveys over the past five decades. Here, we focus on three of the more recent large-scale surveys that are particularly important for the determination of the relative locations of the γ-ray and radio emission regions in AGNs: (*a*) the decades long University of Michigan Radio Astronomy Observatory (UMRAO) blazar polarization survey at

4.8 GHz, 8.0 GHz, and 14.5 GHz (Aller et al. 2017), (*b*) the Caltech OVRO 40-m telescope monitoring survey of 1,158 AGNs at 15 GHz (Richards et al. 2011, Max-Moerbeck et al. 2014), and (*c*) the Max Planck Institute for Radio Astronomy (MPIfR) *Fermi*-GST AGN Multi-frequency Monitoring Alliance (F-GAMMA) monitoring survey of 54 *Fermi*-bright blazars (Fuhrmann et al. 2014). The UMRAO program showed that the linear polarization is generally at the level of a few percent during a flare but can reach as high as 15% in some sources at 14.5 GHz. In the Caltech OVRO 40-m program, the BLLs showed larger variability amplitudes than FSRQs. The F-GAMMA observations show clear migration of flares from high frequencies to low frequencies with time. A recent review of intrinsic variability and interstellar scintillations (ISS) is provided by Jauncey et al. (2016). Intraday variations due to ISS are seen at the 2%–10% level in ∼50% of flat-spectrum radio sources at centimeter wavelengths. A larger fraction of the weaker sources show ISS.

Both the Caltech 40-m and the MPIfR F-GAMMA studies found statistically significant correlations between the radio- and γ-ray-flux density variations in some of the AGNs studied (Richards et al. 2011, Fuhrmann et al. 2014, Max-Moerbeck et al. 2014). In all such cases the centimeter-wavelength radio variations lagged behind the γ-ray variations by about 100 days. The F-GAMMA results also showed that the lag decreases with wavelength, falling to zero by $\approx$100 GHz. It is therefore clear that in some AGNs, the γ-ray emission regions are indeed closer to the SMBH than the radio emission regions. However, there are also observations that show that in some AGNs, the γ-ray and radio emission regions are colocated (Jorstad et al. 2001, Marscher et al. 2011, Jorstad & Marscher 2016, Rani et al. 2018). It appears, therefore, that γ-ray emission from AGNs occurs at a variety of sites, some close to the SMBH and some close to the radio-emitting regions. Nalewajko et al. (2014) have presented an observational plan to locate the sites of synchrotron and Compton emission and argued that spine-sheath jet structure models are not a plausible alternative to external broad emission line photons.

It is instructive to consider the variability in the major energy bands of the archetypal blazar 3C279 shown in **Figure 7**, which is taken from Hayashida et al. (2012). We note that in observing single objects for relatively short periods of a few years, it is very difficult to estimate the significance of any apparent correlations. Here, the emission is discussed in terms of the apparent correlation of variability in the γ-ray and optical bands and the lack of correlation with the X-ray band using the one-zone model, and they show that the variability can be modeled by optical and γ-ray emission components located in the radio-emitting components at distances of several parsecs from the SMBH. However, it is also shown that the observations are consistent with γ-ray/optical emission that is generated much closer to the SMBH.

2.7. Other Jets

There are many other examples of the jet phenomenon. The most similar are the Galactic superluminal sources, produced by stellar mass black holes in binary sources (Mirabel & Rodriguez 1999); SS433 (Abeysekara et al. 2018); γ-ray bursts (Gehrels et al. 2009) (including GW170817; Mooley et al. 2018); pulsar wind nebulae (Durant et al. 2013); and protostellar jets (Bally 2016). Although the physical conditions are quite different in each of these classes of source, common principles are invoked in attempts to model them.

3. JET KINEMATICS AND DYNAMICS

> If, for example, $\gamma = 5$, the apparent diameter of the source will increase by almost 10 light years each year. . .an expanding source could exhibit a rate of increase of flux density high enough to explain the observations.
>
> —M. J. Rees (1966, p. 469)

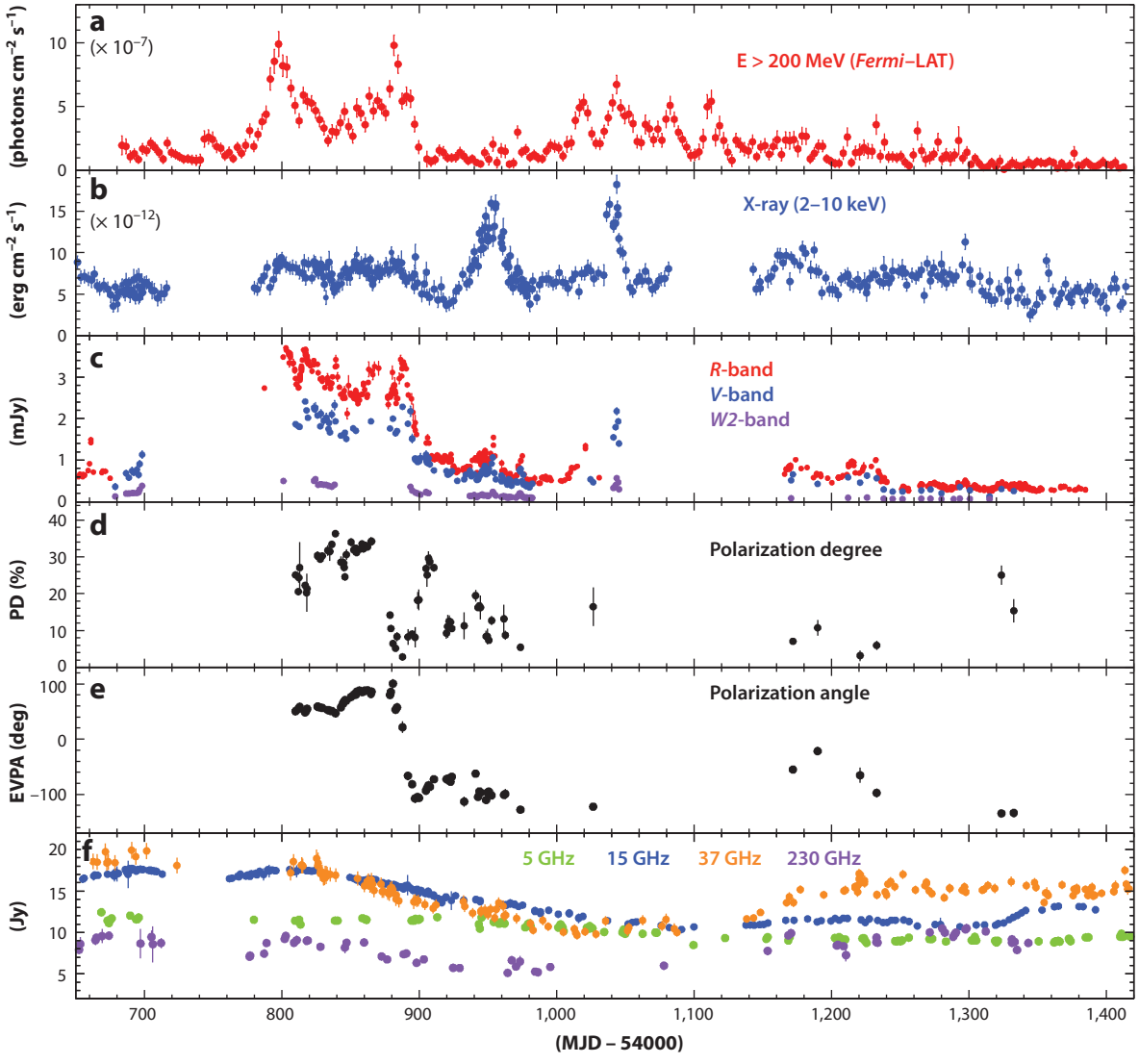

Figure 7

Multiband light curve of 3C279 from August 2008 to August 2010, illustrating the complex nature of the variations in the different bands and the challenge in associating variability in one band with that in another given that more than one zone must often be responsible for the radiation in even a single band, and that there can be different light travel times from these zones. Figure adapted with permission from Hayashida et al. (2012). Abbreviations: EVPA, electric vector position angle; LAT, Large Area Telescope; PD, polarization degree.

3.1. Dynamics and Energetics of Extended Sources

The energy released by the formation, growth, and slowing down of black holes is a major contribution to the cosmological budget, competitive with that from stars. This frames models of relativistic jets.

3.1.1. Energy generation in the galactic nucleus: black holes and accretion disks. It is generally believed that an SMBH exists at the center of nearly all large galaxies with a significant

central stellar bulge (Kormendy & Ho 2013). In all such galactic nuclei, gas will eventually, through various means, make its way from the outer galaxy to the vicinity of the SMBH. The gas can come from a merger with a gas-rich galaxy; the galaxy's own ISM; gas shed by red giants, supergiants, and supernovae; and the tidal disruption of stars that venture inside the SMBH's tidal radius. The gas will have an angular momentum about an initial axis determined by parameters external to the SMBH. However, if the SMBH is spinning rapidly, the gas will tend to orient in the latter's equatorial plane near the hole, forming an accretion disk. When in a steady state, the rate of matter inflow toward the SMBH in this disk is given by the parameter $\dot{M}$ in units of mass per unit time, which is often scaled to the Eddington accretion rate (see the sidebar titled Black Hole Accretion). It is generally convenient to describe the state of the plasma using plasma β parameters, which normalize the pressure of various components to the magnetic pressure.

β: ratio of a pressure or a partial pressure to the magnetic pressure

There are two ways for a jet to be formed by a spinning, accreting black hole: the disk and the spinning black hole itself (see the sidebar titled Electromagnetic Effects). If a Shakura & Sunyaev (1973) type disk surrounds the hole, the disk and hole jet luminosities are given by $L_{\rm d} \sim 0.5\, L_{\rm Edd}\, \dot{m}^2$ and $L_{\rm h} \sim 0.5\, L_{\rm Edd}\, \dot{m}^2 j^2$ (Meier 2012) for near-Eddington accretion rates. If a black hole in the range $M \sim 10^{8-10}$ $M_\odot$ is spinning rapidly, and its accretion rate is, say, half the Eddington limit, in principle both these mechanisms are capable of generating jet powers of $\sim 10^{45-47}$ erg s^{-1}. Over a lifetime of, say, 10^7 years, such a jet can pump up to $\sim 10^{59-61}$ erg into the radio lobes.

3.1.2. Possible accretion states in AGN black holes. While we do not discuss jets in black hole systems with lower mass (e.g., X-ray binary systems) in any detail here, it is very instructive to review accretion states in these systems (which can be observed over many accretion timescales) and how these states relate to jet production in these systems. Black holes of 3–30 $M_\odot$ are observed to have four main accretion states. At the lowest accretion rates, the disk exists in the low/hard (L/H) state, where it is very geometrically thick and optically thin; in this state, the BH system is frequently associated with a weak, steady jet. At higher accretion rates, the disk enters the high/soft (H/S) state, where the accretion inflow is geometrically thin and optically thick; jets are rarely, if ever, seen in the H/S state. When the accretion rate approaches the Eddington value (see the sidebar titled Black Hole Accretion), the very high/unstable (VH/U) state is seen, in which the inflow displays complicated time-dependent behavior, sometimes entering a soft substate for a long time and then briefly entering a hard substate and producing a jet. Finally, at accretion rates significantly above the Eddington value, the accretion inflow produces a strong, optically thick, radiation-pressure-driven wind that can enshroud much of the system and look like a supersoft X-ray source.

Detailed, time-dependent models and simulations of these four states, and transitions between them, are not yet available. But if one can appeal to simple scaling models, one can suggest how they relate to accretion disk theory: The L/H state occurs for $\dot{m} < \dot{m}_{\rm A}$, the H/S state for $\dot{m}_{\rm A} < \dot{m} < \dot{m}_{\rm I}$, the VH/U state for $\dot{m}_{\rm I} < \dot{m} < 1$, and the super-Eddington state for $\dot{m} > 1$ (see the sidebar titled Black Hole Accretion). AGNs should then have only three accretion states: L/H, VH/U, and super-Eddington. In these models, the truly radio-silent H/S state disappears because of the mass dependence of $\dot{m}_{\rm I}$. Low-luminosity AGNs and FR-I sources then would be expected to be in the L/H state and produce a weak steady radio jet. High-luminosity AGNs (Seyferts and quasars) then may be examples of the VH/U state, usually in a soft substate, but entering a hard state for a relatively short time and producing a radio jet, on a cycle time of potentially hundreds to millions of years (Meier 2012). Detailed simulations of accretion flows around black holes over a wide range of mass and accretion rate, plus observations of intermediate mass black hole ($100\, M_\odot < m < 10^5\, M_\odot$) accretion state behavior, could shed light on these somewhat preliminary concepts for AGNs.

The EHT M87 observations (Section 2.2.3.1) suggest an extreme model of this source, where the bolometric power of the putative accretion disk (Akiyama et al. 2019b) is $\sim 4 \times 10^{-8} L_{Edd}$ (Prieto et al. 2016). (If M87 were to radiate at its Eddington limit, it would be as bright as Vega.). By contrast, the power carried by the jet is estimated to be at least 10^{43} erg s^{-1}, at least 300 times more than the disk power (Akiyama et al. 2019). It is difficult to understand how such a powerful jet could be created by an invisible, differentially rotating, accretion disk. If, alternatively, the power derives from the spin of the hole, then the magnetic field must exceed $\sim$1 kG. The electrons emitting at 230 GHz must then have energies $\lesssim$10 MeV, which is also the lower bound on their energy given the measured brightness temperature. Given this field, the radiative cooling time is $\lesssim$30 s. Using the volume of the emitting ring, $\sim 10^{48}$ cm^3, and the millimeter luminosity, the ratio of the pressure of the emitting electrons to the magnetic pressure is $\sim 10^{-11}$. While these emitting electrons are accompanied by cooler plasma and their filling factor could be small, it is also hard to understand how an ion torus could be massive enough to confine the magnetic field and not be observed.

A simpler explanation (see the sidebars Black Hole Accretion and Classical and Revisionist Accretion Disk Theory) is that EHT is observing dynamically insignificant relativistic plasma orbiting with the angular velocity of an ordered magnetic field, confined by a much larger ejection disk. Polarization observations should be prescriptive.

3.1.3. Energy dissipation in the jet and extended lobes. Energy dissipation via particle acceleration and radiative emission is covered in detail in Section 4. We discuss only a few key points here to complete the process from energy generation at the black hole, transport of that energy to regions at distances ranging from milliparsecs to megaparsecs, and finally, dissipation of that energy at those sites.

Observations discussed in Section 2 indicate that momentum can be lost to the surroundings and energy can be dissipated all along a jet from black hole to lobes. However, in many FR-I jets, a great deal of dissipation apparently occurs at a probable recollimation shock near R_{inf}. Astoundingly, however, even though the jet is often slowed there to moderately relativistic speeds, it continues to carry energy to sites that are orders of magnitude further in distance, especially in electromagnetic and particle forms. This is evidenced by the large amount of emission in the Galaxy and lobe jets and the lobes themselves (**Figure 1**).

FR-II jets are equally mysterious. While their black hole jets are certainly accelerated and collimated by electromagnetic means, by the time the lobe jets reach the hot spots and lobes, they behave and emit in a manner very similar to how a supersonic gas jet would. That is, somewhere between the black hole jet region and the lobe jet region, a jet like that in Cygnus A (**Figure 4**) must have lost much of its electromagnetic energy. Most of the energy dissipated in FR-II lobes, therefore, appears to be kinetic—from a still highly relativistic flow.

Both FR-I and FR-II jets dissipate much of their energy in the lobes. However, the FR-Is appear to lose much of their kinetic energy in or near the black hole jet but keep much of their electromagnetic energy well beyond. The FR-IIs behave oppositely, losing much of their electromagnetic energy in or near the black hole jet region, but keeping much of their relativistic kinetic energy out to the lobes. This pattern is broadly consistent with black hole jets being decelerated by a slower, collimating MHD disk wind. The wind decelerates the jet in FR-Is and vice versa in FR-IIs (Begelman et al. 1984).

GRMHD: general relativistic magnetohydrodynamics

3.2. Numerical Simulations of Jets

Much of our current understanding of the formation of relativistic jets derives from 3D general relativistic magnetohydrodynamics (GRMHD) simulations (e.g., Meier 2012, Nakamura et al. 2018)

though much is also being learned from special relativistic and lower dimensionality simulations. Many simulations also include radiative transfer and dissipative processes (Qian et al. 2018, McKinney et al. 2014).

3.2.1. Short history. Some historical simulations are still worthy of note. Norman et al. (1982) performed a 2D hydrodynamic simulation of a supersonic jet propagating through a uniform density medium. The detailed results confirmed the Blandford & Rees (1974) jet hot spot picture of a Mach disk, contact discontinuity, and bow shock forming the jet head, with hot post-shocked jet material surrounding the advancing jet. This picture readily explains the lobe structure of Cygnus A and other FR-II sources.

Lind et al. (1989) and Clarke et al. (1986) performed similar simulations, but with a 2D-MHD code and a strong helical magnetic field encircling the jet. Again, a Mach disk/bow shock structure formed, but there were two distinctive differences. The shock appeared to regularly eject supersonic components/shocks downstream, and the shocked jet material formed a downstream nose cone or plug ahead of the original jet. Such behavior was not seen in hot spots of FR-II sources many kiloparsecs from their SMBH, but it appears to be similar to time-dependent evolution of parsec-scale VLBI sources—in a possible recollimation shock near $R_{\rm inf}$. Mignone et al. (2010) performed 3D relativistic magnetohydrodynamic simulations of a similar situation and found that the helically magnetized jet develops a strong kink instability, which inhibits the forming of a nose cone. However, there are several ways in which nature can avoid or mitigate the kink instability in Poynting jets (Nakamura & Meier 2004): The jet is propagating through a decreasing-pressure atmosphere or the jet plasma is spinning faster than its internal Alfvén speed. Indeed, the M87 black hole jet is clearly Poynting-dominated, accelerating and collimating over ∼300 pc, and yet does not kink until well beyond HST-1.

3.2.2. Jet launching. Several models for jet formation and collimation have been eliminated by recent advances in high-resolution VLBI and the discovery of rapid γ-ray variability, Despite this, different mechanisms could be at work in different nuclear environments.

3.2.2.1. From sub-Eddington accretion disks. Most simulations of jet launching involve radiatively inefficient (very sub-Eddington) accretion flows around rotating black holes—the type that one would expect in the engines of FR-I and weaker sources. From the tour de force 2D- and 3D-GRMHD simulations (De Villiers & Hawley 2003, Gammie et al. 2003, McKinney 2006), it is clear that accreting, rotating black holes can produce jets and that the jet power is an increasing function of the SMBH spin.

3.2.2.2. From super-Eddington accretion disks. Rather rare sources that are thought to be accreting above the Eddington limit, e.g., broad absorption line quasars, are known to be less radio loud than the main quasi-stellar radio source (QSR) population—but not radio silent. It would seem, then, that even with a large, geometrically thick, radiation-pressure dominated disk, such objects still can produce jets. These ideas have been investigated by Sadowski et al. (2014), Sadowski & Narayan (2015), McKinney et al. (2014, 2015), and Qian (2018) using a 3D-GRMHD code that includes radiation MHD of disks with $\dot{m} \sim 20$ and 50. They find that the radiation and jet emerge from a geometrically beamed, bipolar region, with super-Eddington isotropic luminosities. (That is, the total radiation and jet luminosity is of order Eddington, but much of it is beamed in a narrow polar funnel.) As expected, the super-Eddington wind carries away a significant amount of jet energy, but nevertheless a jet is produced. In addition, the heart of the jet engine can be seen down the funnel by an observer if the viewing angle is small enough.

3.3. Jet Confinement

A long-standing question about AGN jets is how they are confined and collimated. This question likely has different answers at different radii. If we accept that the jet originates from close to the black hole, then it has been most commonly assumed that the jet is initially confined by the walls of a funnel formed by an ion-supported torus. However, this may not be present and, in any case, cannot extend to large distances where we still see jets being collimated. A gas dynamical disk wind may confine the black hole jet close to the hole (Globus & Levinson 2016). Alternatively, if the wind is hydromagnetic, then the jet may carry an axial current I which supports a toroidal magnetic field $B_\phi \sim 0.3\,(I/1\,\mathrm{EA})(r/1\,\mathrm{pc})^{-1}$ G, for $r \geq r_{\rm jet}$ (e.g., Begelman et al. 1984; Levinson & Globus 2017; Section 3.1.2). Ultimately, at a large enough cylindrical radius $r_{\rm out}$, which may lie within the wind, there will be a return current and the outward magnetic stress must be balanced by gas pressure (Begelman et al. 1984). However this pressure will be $\sim(r_{\rm out}/r_{\rm jet})^{-2}$ smaller than the pressure in the jet. As discussed, the galaxy jet is probably directly confined by gas pressure, and in the lobes, in the case of FR-II sources, by the backflow of jet plasma that has passed through the hot spot shock.

3.4. Jet Propagation and Shock Behavior

As we discussed above, multidimensional simulations with a strong helical magnetic field are particularly applicable to the structure and evolution of parsec-scale radio sources, especially near the jet collimation break (**Figure 3**). As further evidence, 1.5D-RMHD jet simulations, also with a strong helical magnetic field, have been applied to the time-dependent structure of HST-1 in M87 (Nakamura et al. 2010). In contrast to hydrodynamic simulations of jet flow, however, if the jet speed is supermagnetosonic in both the ambient medium and internally in the jet flow itself, the 1.5D-RMHD results show that two bow shocks and two Mach disks form in the flow. The leading bow shock is a fast-mode magnetosonic shock, and the one behind it is a slow-mode magnetosonic shock. Conversely, the leading Mach disk, somewhat behind the forward-slow bow shock, is a reverse-slow shock. And, finally, a reverse-fast Mach disk trails the reverse-slow Mach disk. This quad-shock system is seen in HST-1 outbursts and can be fit with just a few parameters to a supermagnetosonic jet impacting a slower one from behind (Nakamura et al. 2010).

Furthermore, the shock angular momentum conservation condition induces plasma rotation between the two bow shocks and then also between the two Mach disks, with the two intershock regions rotating in opposite directions. Such a behavior may explain oppositely directed polarization rotations in blazars like OJ287, which has a viewing angle of only 2° (Cohen et al. 2018).

4. EMISSION MODELS

> The observations by Baade (1956) of the polarization of the jet in M87 are convincing proof of the hypothesis that this optical radiation emitted by the jet in M87 is strongly polarized—and thus is synchrotron radiation. . .total energies in the range $10^{56}-10^{61}$ ergs are demanded. . .the rate of electron-positron energy generation will be sufficient to balance the loss of energy by synchrotron radiation.
>
> —G.R. Burbidge (1956, p. 416)

4.1. Particle Acceleration

Even if we develop a good model of jet dynamics, this does not tell us how jets radiate and what we should observe. The problem is that we require a choice of emission process and a prescription for evolving the particle distribution function. Most phenomenological investigations and numerical simulations have used ad hoc prescriptions and should be used with caution when comparing

with observations. However, kinetic codes are now being used to start to understand basic particle acceleration processes.

4.1.1. General principles. Jets, and the double radio sources that they supply, are observed throughout much of the entire 70-octave electromagnetic spectrum and, perhaps, beyond. Even if a jet is well modeled at the level of continuum mechanics, we must still explain where and how the emitting relativistic particles are accelerated and how they are transported before they cool. The electron energies for which we have good evidence range from $\lesssim$100 MeV to explain lower brightness and self-absorbed radio cores, to $\gtrsim$100 TeV to explain X-ray synchrotron and γ-ray emission. Much higher energies are invoked in some models (Sections 2.5 and 4.2.2.6). The case for some distributed acceleration along the jet is very strong as adiabatic and radiative cooling will ensure that the surface brightness falls much faster with R than observed.

A charged particle gains energy at a rate eEc when exposed to an electric field of strength E. If the field varies slowly, the acceleration is called electrostatic. This is likely to occur in black hole magnetospheres where charged particles must be created continuously and electrostatic gaps are thought to be involved, though they are likely to be energetically insignificant as the potential difference needed is orders of magnitude smaller than the total available (Levinson & Segev 2017, Chen et al. 2018). Similar structures have been invoked in the black hole jet and may be mandated as the density of charge carriers continues to be inadequate to deliver the current density and space charge required by Maxwell's equations. However, entrained gas will soon make this a nonissue, and electrostatic acceleration is unlikely to explain most of the observed jet emission. When there are more protons than positrons, the protons should take up nearly as much energy as the electrons, but they can be accelerated to much higher energy as their radiative losses are less.

4.1.2. Diffusive shock acceleration. Acceleration at high Mach number shocks has often been invoked as the primary particle acceleration mechanism in jets. This is observed to be very efficient in supernova remnants and at planetary bow shocks. In its simplest version, a strong planar shock with compression ratio r transmits a downstream momentum space power-law distribution function in momentum with slope $3r/(r-1)$, so that a strong shock with $r \sim 4$ will lead to a synchrotron or Compton power law with $\alpha \sim -0.5$, as is often observed (Drury 1983). Weaker shocks can account for steeper-spectrum sources.

The shock should be nonrelativistic and the plasma $\beta \gg 1$ ahead of the shock, and the downstream distribution function must be corrected to allow for the dynamical effect of the relativistic particles on the shock structure, which can decelerate the upstream flow and change the effective heat ratio. Low-β shocks are not compressive, and relativistic shock acceleration probably converts most of the downstream energy into thermal (relativistic) particles. The shocks can accelerate to high energy because a magnetic field is also created at the shock front by the accelerating particles. The maximum energy accelerated should be determined by the shock width or radius of curvature. A further complication is that the very highest-energy particles can escape upstream from a curved shock front, although most accelerated particles will be transmitted downstream and can lose energy during subsequent expansion and radiation. Despite these limitations, shocks remain a good candidate for particle acceleration in galaxy jets, the hot spots, and the radio lobes. In particular, recollimation shocks near $R_{\rm inf}$ may be efficient accelerators (e.g., Marscher 2014).

4.1.3. Relativistic reconnection. Axisymmetric relativistic jets confined by a toroidal magnetic field are prone to nonaxisymmetric kink instabilities that can force oppositely directed field lines together so that they reconnect by exchanging partners (e.g., Begelman 1998, Barniol Duran et al. 2017). This will occur in many comparatively small regions where ohmic dissipation balances

PIC: particle in cell

flux-freezing. Nonrelativistic reconnection is rather inefficient, with most of the dissipated energy going into heating the thermal plasma, although surprisingly large energies may be accelerated. Relativistic reconnection has been investigated extensively using particle in cell (PIC) simulations and can be very efficient in converting magnetic energy, measured in a comoving frame, into ultrarelativistic particles (Sironi & Spitkovsky 2014, Werner et al. 2018).

Simulations of current sheets, which form in magnetized jet flows, show them breaking up into a series of islands separated by X-points where two components of the magnetic vector change sign (Beloborodov 2017). Channels can be formed by the electric vector, which can be locally larger in magnitude than the magnetic field; electrons and positrons are accelerated along the field and then radiate synchrotron radiation at the ends of the channel where they encounter a strong transverse magnetic field. Other acceleration modes have been associated with relativistic reconnection, including scattering within and between islands and small pitch angle acceleration along a guide field lying in the main current sheet.

Shock and reconnection acceleration are associated with surfaces—current sheets. Continuous emission across and along jets and lobes should be observed so long as the electrons do not cool on the shorter of the flow and propagation timescales. However, dynamical features where the field is expected to be strong, and the particle density high, should also be highlighted. In particular the knots in sources like M87 and the hot spots in FR-II lobes are plausibly shocks, while reconnection should be endemic in boundary layers (see Section 2.2.4.3) from the black hole to the lobes. Shocks are expected to exhibit high parallel polarization while boundary layers should show perpendicular polarization. Radio, optical and X-ray polarimetry (Tavecchio et al. 2018) should be quite diagnostic. Shocks and reconnection should be distinguishable through X-ray polarimetry (Tavecchio et al. 2018).

4.1.4. Stochastic acceleration. Supersonic gas dynamical jets are famously noisy, which means that they radiate sound waves. Similar MHD wave emission is expected in AGN jets. These waves are likely to accelerate particles through second-order stochastic processes and mediate a form of local viscosity in the flow (Kulsrud 2004, Stawarz & Petrosian 2008). (Note that a high level of turbulence is likely to inhibit particle transport, especially of radio-emitting electrons with small gyro radii. It can, however, promote reconnection.) Wave acceleration is more likely to be volumetric, contributing to emission within the core of a jet, especially if jets develop large-scale turbulent eddies. It should also be especially effective in boundary layers, though the resulting synchrotron radiation is likely to be less strongly polarized than with relativistic reconnection.

4.1.5. Magnetoluminescence. While these processes may suffice to account for slowly varying emission from jets, they may not be fast enough to explain the most dramatic γ-ray variation seen in jets and other sources such as the Crab Nebula. One possible candidate mechanism is suggested by observations of solar prominences and, perhaps, the Galactic center. The magnetic field in a low-β jet may organize itself into current-carrying ropes that become tangled as the field lines are pulled and twisted by the large-scale jet flow. Discrete ropes can untangle, without topological change, at speeds $\sim c$, creating large, frictional, electric shear stress. The reduction in the magnetic energy should appear as high-energy electrons and ions created on the light crossing time of the reconnecting region (Blandford et al. 2017).

4.2. Radiative Processes

The familiar view of jet emission is that their spectra commonly appear to have a Bactrian form with two humps (**Figure 5**)—the lower peak being associated with synchrotron emission, the

RADIATIVE TRANSFER I

Synchrotron Radiation

A relativistic electron (or positron) with energy $\gamma m_e c^2$ spiraling along a uniform magnetostatic field B (measured in G in a reference frame with no electric field) emits linearly polarized ($\sim$70%) synchrotron radiation with characteristic frequency $\nu \sim \gamma^2 B$ MHz. The electron cooling time is $t_{\rm syn} \sim 5 \times 10^8 B^{-2}\gamma^{-1}$ s (Rybicki & Lightman 1979, Longair 2011). The degree of circular polarization is $\sim 3/\gamma$ for electrons alone. Absorption can be estimated by noting that the brightness temperature satisfies a thermodynamic limit $3kT_{\rm B} = 3Ic^2/2\nu^2 \lesssim \gamma m_e c^2$. When transforming from the source frame to the observer frame, $T_{\rm B}$ transforms in the same manner as ν. Also relevant is the possibility of absorption of radio emission by cool plasma along the line of sight, for example, in an accretion disk. The absorption coefficient at radio wavelengths for this process can be written as $\mu_{\rm ff} \sim 10^{-25}(\langle n_e^2\rangle/{\rm cm}^{-6})(T_e/10^4\ {\rm K})^{-1.35}(\nu/1\ {\rm GHz})^{-2.1}{\rm cm}^{-1}$.

Faraday Rotation

Linearly polarized radio waves that propagate through a magnetized electron-ion plasma can be decomposed into circular polarized eigenmodes, which propagate with slightly different phase velocities so that the plane of polarization appears to rotate after they are combined at the end of the propagation. The angle of rotation can be expressed as $\Delta\phi = RM\lambda^2$, where $RM = 8.1 \times 10^5 \int({\rm d}s/1\ {\rm pc})(n_e/1\ {\rm cm}^{-3})(B_{||}/1\ \mu{\rm G})\,{\rm rad\,m}^{-2}$ is the rotation measure, with n_e being the electron density and $B_{||}$ the parallel component of magnetic field. The wavelength dependence of the rotation allows the product of the field and the density to be estimated around jets.

higher one with Compton scattering of synchrotron photons in low-power sources and external disk and broad emission line cloud photons in high-power sources (Section 2.3). The simplest, one-zone, version of this model is that both humps originate from a single site, plausibly associated with $R_{\rm inf}$, where a recollimation shock may form (see the sidebars titled Radiative Transfer I and Radiative Transfer II). A more complex model brings in variation along the jet. While the Compton-synchrotron model may still capture the main observed features of AGN jets, there are some challenges.

4.2.1. Some current questions. This is an exciting time in the study of AGN jets, and many outstanding questions have been brought into focus.

4.2.1.1. Is the radio emission synchrotron radiation? The radio brightness temperatures should satisfy $T_{\rm B} \lesssim 10^{12}\mathcal{D}/(1+z)$ K in order to avoid catastrophic production of Compton γ-rays (Begelman et al. 1984). This is a strong constraint when the source is resolved and the brightness temperature is directly measured, and there may be instances when it is not satisfied. It is less secure when the linear size is estimated by variability that may be attributable to relativistic kinematics or scintillation.

4.2.1.2. Is the γ-ray emission synchrotron radiation? If we suppose that the electric field strength does not exceed the magnetic field strength, in cgs units, then electron synchrotron radiation photons must have wavelengths more than the classical electron radius, or energies $\lesssim$70 MeV (Landau & Lifshitz 1975). However, if electrons are created hadronically at very high energy, they can simply cool, emitting more energetic photons.

4.2.1.3. Can jets transition rapidly from electromagnetic to particle dominance? In many sources, the flux from the Compton peak significantly exceeds that from the synchrotron peak,

RADIATIVE TRANSFER II

Inverse Compton Scattering

A relativistic electron (or positron) in a jet can collide with an ambient soft photon according to the Thomson cross section, $\sigma_T \sim 7 \times 10^{-25}$ cm^2. The photon may be emitted by the jet itself, by stars, by the accretion disk, or by gas clouds. The photon frequency/energy is Doppler-boosted once from the frame of the soft photon to the electron rest frame and then a second time from the rest frame back to the original frame, by an average factor $\sim\gamma^2$, with the numerical coefficient dependent upon the angular distribution of soft photons. This suffices to compute the emissivity, with the caveat that if the scattered photon energy approaches that of the electron, Compton recoil is important and the emissivity is diminished. Below this Klein–Nishina limit, if we define an effective magnetic field strength that would have an energy density equal to that of radiation field, then the electron cooling time is similar to that for synchrotron radiation. The requirement that the γ-ray flux from the radio source in the jet not exceed what is observed limits the synchrotron radio brightness temperature to $\sim 10^{12}$ K, ignoring Doppler boosting.

Pair Production and Annihilation

When a γ-ray with energy $h\nu_\gamma$ encounters a soft photon head-on with energy $>m_e c^4/h\nu_\gamma$, there is enough energy to create an electron-positron pair. The cross section for this process is $\sim 0.2\sigma_T$. In practice this provides a lower bound on the radius where γ-rays are produced in an AGN jet. The inverse process is annihilation of electrons and positrons, which proceeds with a cross section $\sim\sigma_T(c/v_e)$, where v_e is the electron thermal speed.

implying that $\beta_{rad} \gg 1$ and $\beta_e \gg 1$. By contrast, we have emphasized a scenario in which jets are powered electromagnetically by a spinning black hole where the opposite inequalities should be satisfied.

4.2.1.4. Do γ-rays originate from jet radii $\lesssim$1,000 r_g, or are there bulk Lorentz factors $\gtrsim$100 in the flow? Variation in some γ-ray jets with timescales $\lesssim\tau_g$ (Section 2.3) suggests that much larger Lorentz factors are present than indicated by observations of superluminal motion, and the emitting volume is very compact while still being large enough to account for the observed flare fluence.

4.2.1.5. Is there something seriously wrong with our basic model of accretion in AGNs? There is a firm lower bound to the radius from which γ-rays of energy E_γ can escape called the gamma-sphere (Levinson & Blandford 1995). This is the surface where the optical depth to pair production on photons with energy $\gtrsim m_e^2 c^4/E_\gamma$ is unity, where the cross section $\sim 0.2\sigma_T$. Geometrical corrections can soften this constraint somewhat and, in the case of BLLs, we can argue that the accretion disks are dark. However, the radiation field is well-measured in a quasar like 3C279, which displays minute-scale GeV variation (**Figure 7**).

4.2.2. Alternative emission models. In view of these problems, several alternative emission models have been entertained.

4.2.2.1. Proton synchrotron radiation. This has been associated with compact radio sources, X-ray jets, and hot spots mainly because the lifetime of a particle with mass m emitting at a given frequency in a given field $\propto m^{5/2}$ (Petropoulou & Mastichiadis 2012). Although short-lived in their rest frames, ultrarelativistic pions and muons produced by hadronic processes can also contribute to γ-ray synchrotron emission.

4.2.2.2. Curvature radiation. The challenges of high-brightness electron synchrotron sources can be obviated by invoking coherent emission processes. In particular, curvature radiation, in which bunches of electrons stream in a long, curving magnetic field, produces brightness temperatures limited by the total energies of the bunches—a mechanism that has been invoked in pulsars. A serious constraint that these models should satisfy is that high-brightness emission not be degraded by nonlinear transmission effects, including induced Compton scattering and stimulated Raman scattering (Levinson & Blandford 1995). Curvature radiation has also been invoked to explain γ-ray emission (Bednarek 1997).

4.2.2.3. Cyclotron masers. Alternatively, the brightness temperature limitation can be broken with relativistic electrons if there is a population inversion and the emissivity declines with increasing particle energy. This can happen with cyclotron emission by mildly relativistic electrons due to the dependence of the cyclotron frequency on the relativistic mass. This is observed in Jovian decametric emission (Begelman et al. 2005).

4.2.2.4. Plasma waves. Shocks and magnetic discontinuities can produce large current densities that may radiate large-amplitude plasma modes, which may, in turn, mode-convert into electromagnetic radio waves as seen in solar radio bursts.

4.2.2.5. Proton-pion production by energetic protons. Another widely discussed possibility for the γ-ray emission is that it is hadronic (Muecke et al. 2003, Reimer 2012). The basic idea is that most of the energy dissipated in the jet goes into protons (not pairs) and that these are accelerated relatively rapidly to PeV or even EeV energies, where they can undergo a variety of interactions and create showers like cosmic rays hitting our atmosphere. The first processes considered were p-p collisions, which could happen if, for example, a jet moved to encounter a dense molecular cloud.

4.2.2.6. Photo-pion production by energetic protons. Pions may also be produced by collisions with photons (Muecke et al. 2003). To give one example, consider an FSRQ with spectrum peaking at $\sim$30 meV, or roughly 30 μm. Suppose that the jet has a Lorentz factor $\Gamma \sim 10$ so that the background photons have energy $\sim$10 meV. Now suppose that protons can be accelerated to energies $\sim$500 PeV in the jet frame. The photons will have energies $\sim$150 MeV in the proton rest frame, just above the threshold for conversion to neutrons with pion production. This will proceed with a cross section $\sim 10^{-4}\sigma_{\rm T}$. Roughly $m_{\rm p}/m_\pi \sim 10$ pions must be made to extract all the proton energy. Charged pions will decay into muons, neutrinos, electrons, and positrons, which can emit synchrotron and Compton radiation. Typical electron energies are $\sim$100 PeV in the AGN frame. The neutrinos are relevant to their possible detection (Section 2.5). Neutral pions will decay directly into $\sim$1 EeV γ-rays, which will quickly cascade into pairs and lower-energy γ-rays until the latter can escape. The neutrons will escape the jet before decaying back to protons. Overall, the process is quite inefficient as the cross section is low and, typically, no more than a few percent of the initial proton energy will emerge as γ-rays for each pion created (Böttcher et al. 2013). Also, this could raise the integrated density of SMBHs to unreasonable levels (Yu & Tremaine 2002).

4.2.2.7. Photo-pair production in a shielded jet. In order for $\sim$1 GeV photons to escape from close to the hole in an FSRQ and vary rapidly, it is necessary to exclude UV and soft X-ray photons. One way to do this is if there is a disk wind at small radius driven by radiation and magnetic fields that forms a sheath around the inner jet that can absorb essentially all of the external photons shortward of the Lyman continuum (Meyer et al. 2018). The mass flow needed is modest, but

the gas would have to cool fast enough to have a large enough neutral fraction (Königl & Kartje 1994). Under these circumstances, the hardest photons would have energies $\sim 100\,\mathrm{eV}$ in the jet frame. The cross section for photo-pair production rises from zero at threshold, when the photon energy is $\sim 1\,\mathrm{MeV}$ in the proton rest frame, to $\sim 0.01\sigma_{\mathrm{T}}$ when the energy is $\sim 100\,\mathrm{MeV}$ before pion production sets in. An accelerating proton will therefore be subject to increasing radiative drag as its comoving frame energy approaches $\sim 1\,\mathrm{PeV}$, and ~ 50 TeV pairs will be produced. If the jet is highly magnetized at this radius, as we are otherwise assuming, the pairs will cool rapidly by synchrotron emission of photons with energy $\sim 10\,\mathrm{GeV}$ in the AGN frame. These are just able to escape. As the photon density and cross section are both larger than with pion production, it is possible to convert the electromagnetic energy dissipated into GeV γ-rays from the inner jet with very high efficiency.

4.3. Jet Emission Profile

We are a long way from being able to model the observed intensity distribution of AGN jets, and indeed we use it, in combination with simulations, to try to infer the physical conditions and the acceleration and emission processes. Despite this, there are some key effects that either have been seen or should now be accessible to observation.

4.3.1. Radio core-shift. The unresolved radio core has generally been associated with self-absorbed synchrotron radiation from the approaching jet. We are, in effect, looking at a radio photosphere formed by the jet walls and a surface across the jet. The size of the unresolved photosphere should scale roughly as the wavelength and the size that can be resolved interferometrically with an intercontinental baseline. This expectation is consistent with multifrequency VLBI observations. However, we expect to see the unresolved centroid of the photosphere shift toward the position of the black hole with increasing ν (Blandford & Königl 1979, Königl 1981). This effect has been seen (Plavin et al. 2018).

4.3.2. Radio-γ-ray cross correlation. The statistical evidence that the γ-rays vary before the radio emission suggests that the variable γ-ray emission site lies within the radio core (Section 2.6), allowing us to discriminate between models.

4.3.3. Gammasphere. Likewise, if the γ-ray variation is dominated by activity at the gammasphere (Section 4.2.1.5), with radius increasing with photon energy, then we would expect low-energy variation to precede high-energy changes. Alternatively, if γ-ray variation is due to hadronic showers in an optically thin region, then we might expect the opposite ordering. However, there is not yet strong evidence either way.

4.3.4. Knots in M87. Important clues concerning general jet dynamics and radiation properties have been drawn from a few well-resolved X-ray and optical jets (Section 2.4). The six M87 knots have been interpreted as strong, particle-accelerating shocks, which would indicate that $\beta \gtrsim 1$ (Biretta et al. 1999). They have also been interpreted as places where the jet velocity turns toward us (Bicknell & Begelman 1996). Given the successful observing campaign involving HST-1, it may be possible to extend this to the innermost knots.

4.3.5. Rapid variability. Variability from optically thick radio emission through TeV γ-rays provides important constraints on physical conditions within jets; the associated timescales are sometimes $\lesssim r_{\mathrm{g}}/c$, which has motivated discussion of extra Lorentz factors and spatial focusing of

jets. Symmetric and nonsymmetric variations, lags, and orphan flares have been identified (Potter & Cotter 2015).

4.3.6. Lessons from double radio sources. There is also much to be learned from observations of extended radio sources that may be scalable to smaller-scale jets and CSOs (Section 2.2.4). Comparison of X-ray and radio images of Cygnus A are essentially hydrodynamical, with $\beta \gg 1$, and are able to account for the jet-terminating hot spots, which dance about like a dentist's drill (Scheuer 1982), as well as the backflow and a large cocoon enveloping the whole galaxy in pressure equilibrium with the surrounding gas and permeated by weak shock fronts. However, the large linear polarizations reported in many lobes suggest that magnetic stress is important and $\beta \sim 1$.

5. AGN JETS AND THE UNIVERSE

> The value of N/N_m found for our sample of thirty-three 3CR sources is 0.75. This is in direct conflict with the value of 0.50 required by a steady state [universe] in which no evolutionary effects are admitted.
>
> —M. Schmidt (1968, p. 405)

5.1. Radio-Loud/Radio-Quiet Dichotomy

The classification of AGNs, like the classification of stars, has evolved with the compilation of multiwavelength data and partial success in relating the taxonomy to physical characteristics of the sources (e.g., Meier 2012). Essentially all bright galaxies contain SMBHs that may become active. Now, roughly 10% of optically selected quasars are RLQs (Ivezić et al. 2002, Kellermann et al. 2016). Jets are not always observed in these sources but are presumed to be present. The remaining roughly 90% are RQQs, though not silent (Barvainis et al. 2005). This, the simplest classification of active galaxies, is summarized in **Table 3**.

From the perspective of optical spectroscopy, AGNs are characterized by their line emission, which is commonly split into broad and narrow components (Hine & Longair 1979, Jackson & Wall 1999, Osterbrock & Ferland 2005). The absence of broad lines from Seyfert type 2 galaxies/narrow-line radio galaxies is attributed to obscuration of a broad-line region by dusty gas associated with a thick or heavily warped outer disk, or torus; an outflowing wind; or inflowing gas. Therefore, for these objects, the observer inclination θ is large with respect to the black hole spin, presumed here to be aligned with the disk angular momentum and the jet, when present (Urry & Padovani 1995, Meier 2012). Weak, polarized, back-scattered broad lines are observed from Seyfert type 2 galaxies/narrow-line radio galaxies, which supports this explanation (Antonucci &

Table 3 Classification of AGNs by their optical properties

Abbreviation	Expansion	Definition	Density (L_{bol})[a]
LINER	Low-ionization nuclear emission-line region	Weak Seyfert-like galaxy	$\sim 10^{6.5}$ ($<10^{42}$)
Sy 2	Seyfert galaxy type 2	AGN with narrow permitted & forbidden lines	$\sim 10^{5.3}$ ($>10^{42}$)
Sy 1	Seyfert galaxy type 1	AGN with broad permitted & narrow forbidden lines	$\sim 10^{5}$ ($>10^{42}$)
QSO	Quasi-stellar object	Powerful AGN that outshines its host galaxy	$\sim 10^{2.5}$ ($>10^{45}$)
WLRG	Weak-line radio galaxy	Radio galaxy analog to LINER	$\sim 10^{4}$ ($<10^{42}$)
NLRG	Narrow-line radio galaxy	Radio galaxy analog to Sy 2	$\sim 10^{1.2}$ ($>10^{42}$)
BLRG	Broad-line radio galaxy	Radio galaxy analog to Sy 1	~ 10 ($>10^{42}$)
QSR	Quasi-stellar radio source	QSO with strong radio emission	$\sim 10^{-1.5}$ ($>10^{45}$)

[a]Density is in units of Gpc^{-3}, local; AGN L_{bol} is in erg s^{-1} (Tadhunter 2016). Bright field galaxy density is $\sim 10^{7}$.

Miller 1985). Optically, RLQs and RQQs are intrinsically similar, with similar masses and accretion rates.

Magnetically arrested disk: the central magnetic flux holds back inflowing gas

Magnetically choked accretion flow: inflowing gas leads to an enhancement of hole magnetization

One possible reason for a quasar forming a powerful jet and becoming radio loud is that the SMBH is spinning rapidly. Observations of black hole X-ray binaries support the view that spin is necessary for jet production (Narayan & McClintock 2012). However, many Seyferts with large measured spin are radio quiet (Reynolds 2014), and, using the Soltan (1982) argument, Yu & Tremaine (2002) and Elvis et al. (2002) have argued that most RQQs spin rapidly. It appears that black hole spin is also insufficient for jet production. This is referred to as the spin paradox. It implies that a second, independent factor must be invoked to explain why a fraction $\sim 10^{-4}$ of local AGNs, rising to ~ 0.1 of high-redshift quasars, should produce jets and become radio loud largely independent of how the optical emission is produced.

One explanation (Section 3.1.2), which underpins most numerical simulations, is that the gas supply rate is either too slow or too fast to allow the accreting gas to cool and form a large torus and funnel to collimate the jet. A long-standing concern with this explanation is that it requires the arrangement to persist for $\gtrsim 10$ Myr, the lifetime of a radio source. Given the observed rapid variability in AGNs, it seems hard to believe that the accretion rate is that stable. A second worry is that we now observe jets being collimated at altitudes, $r_g \ll r \ll R_{inf}$, that are too large for a thick accretion disk to be important and too small to be associated with the ISM.

5.1.1. Disk magnetization. It is clear that disk magnetization is a key factor in jet production. There are two aspects to this, which are described in the following.

5.1.1.1. Near magnetization. The existence of the MRI ensures that disks are strongly magnetized. However, it does not guarantee that there is a permanent, large-scale vertical field threading the disk and the SMBH in radio-loud but not radio-quiet AGNs. A flux large enough to produce a magnetically arrested disk or a magnetically choked accretion flow will hold up the flow outside the r_{ISCO}, will generate more powerful jets, and may even be strong enough to suppress the MRI for a while (Narayan et al. 2003, McKinney et al. 2012). One variation, reviewed by Meier (2012), is that the disk is counter-rotating with respect to the spin in radio-loud AGNs, allowing more flux to accumulate within the ISCO. However, this conjecture was not supported by simulations (Tchekhovskoy et al. 2011, Tchekhovskoy & McKinney 2012).

Stellar black holes like GRS 1915+105 (Mirabel & Rodriguez 1999) can provide further insight. This source produces powerful, intermittent jets when the accretion rate is near Eddington and when the source passes through the jet line in the X-ray hardness–intensity diagram, which it does every 20 min with a duty cycle ~ 0.06 (Fender et al. 2004). This is attributed to a disk instability causing a hot, ADAF-like structure that persists for an inflow timescale and is capable of creating a large field through dynamo action (Meier 2012). Unfortunately, there is no evidence of this cycling on timescales that should increase in proportion to mass over thousands of years in AGN jets. Furthermore, the fact that being radio loud or quiet appears to be a long-term feature makes it hard to associate with instabilities that grow on a dynamical timescale close to the black hole.

A rather different mechanism that may operate in the presence of radiation pressure, and which addresses this problem, is that a physical dynamo continually regenerates a field of fixed polarity—the sign of $\vec{\Omega} \cdot \vec{B}$—near the inner accretion disk (Contopoulos et al. 2018). This could be due to radiation pressure acting on electrons combining with the MRI, which expresses no such preference. This should be testable.

5.1.1.2. Distant magnetization. A possible clue is that radio sources are mostly associated with elliptical and not spiral galaxies. This suggests that it is the environment at radii $r \gtrsim R_{\rm inf}$ that is responsible for the dichotomy. The large-scale gas inflow in a spiral is likely to be mostly equatorial, and it may be hard to build up and trap magnetic flux within $R_{\rm inf}$ as the field lines become radial on the surface of the galaxy disk and may quickly reconnect and escape.

By contrast, in an elliptical galaxy, the inflow derives from the circumgalactic medium and should be quasi-spherical. Magnetic flux can accumulate and be effectively trapped within a large funnel with radius $\gtrsim R_{\rm inf}$ formed by hot gas settling onto the nucleus at a rate $\dot{M}$ and extending to high latitude. The magnetic stress at $R_{\rm inf}$ would balance the ram pressure of the infalling gas. The accretion disk could concentrate the field near the spinning black hole, and making the simplest assumptions, we find that the electromagnetic power of the spinning black hole would be $\sim \dot{M}\sigma c j^2$. A similar power would be associated with a hydromagnetic wind leaving the inner accretion disk. The actual accretion rate onto the black hole could be much smaller than the infall rate (Section 2.1.1) and the innermost disk could be magnetically dominated (Section 3.1.2).

5.2. Fanaroff–Riley Classification of Extended Radio Sources

The Fanaroff–Riley classification associates edge-brightened lobe morphology with high-power sources and edge-darkened morphology with low-power sources.

5.2.1. Compact and extended radio sources. As described above, starting from the earliest unification theories and unifying observations of the 1960s and 1970s, the view has been developed that compact and extended radio sources are intrinsically similar, but in the former case a relativistic jet is pointed toward us, and in the latter, it is not. As predicted, compact radio sources—more generally, blazars—have faint extended halos, their unbeamed lobes. Likewise, extended radio sources have faint cores identified with the nuclei of their host galaxies. This bold unification implies that both types of source have similar distributions of intrinsic jet and environmental properties.

5.2.2. Physical origin of the Fanaroff–Riley classification. The FR class of the extended sources (Section 1.1, **Table 1**) remains an impressively striking feature of the observations. Physically, what seems to be happening is that jets with power $\gtrsim 5 \times 10^{45}$ erg s^{-1} (Potter & Cotter 2015) are able to escape the galactic nucleus with little deceleration by the surrounding and confining medium or a magnetic sheath, a slower disk wind, or a settled ISM. The opposite is true for lower-power jets, and once they start to decelerate, they are quickly converted into subsonic plumes that fade with radius and inflate buoyant bubbles (**Figure 1**). We know that FR-I jets are initially relativistic and that the observed characteristics that determine if a blazar is classified as a BLL or an FSRQ emanate from radii $\lesssim R_{\rm inf}$ (Kharb et al. 2015). We also observe that when the transition occurs, it does so far inside the galaxy's core radius (see Bicknell 1995). The existence of hybrid-morphology radio galaxies—which have an FR-I jet on one side of the galaxy and an FR-II jet on the other—also supports FR-I jets being formed near $R_{\rm inf}$.

From a fluid point of view, $R_{\rm inf}$ is a very natural location to change the nature of a flow as there is an abrupt change in the gradient of the gravitational potential and, therefore, in the external pressure gradient (Levinson & Globus 2017). A recollimation shock may form and disrupt a low-power jet (Asada & Nakamura 2012). Alternatively, a highly magnetized jet may be subject to a disruptive kink or helical instability (Tchekhovskoy & Bromberg 2016).

The major change in an FR-II jet is that it appears to be strongly magnetized when formed but then declines—the best-studied hot spots where these jets terminate are best modeled by a weakly

magnetized upstream flow that accelerates electrons up to ∼1 TeV and amplifies the field up to ∼100 μG (Werner et al. 2012, Araudo et al. 2018). The dynamical decline of the jet magnetic field could be abrupt if recollimation induces turbulence that facilitates magnetic reconnection and dissipation (Meier 2013).

5.3. Blazar Sequence

In the optical, BLLs show, at most, weak lines, while FSRQs have strong, broad lines. This is usually attributed to a change in the accretion mode from thick, radiatively inefficient inner disks to thin, radiatively efficient disks radiating most of their power in the UV, although there is a possibility that radiative inefficiency is due to dominant, external magnetic torques extracting most of the angular momentum (see the sidebars titled Black Hole Accretion and Electromagnetic Effects).

When we turn to the beamed jets, the BLLs/FSRQs are generally unified with beamed FR-I/II sources (Section 1.1, **Tables 1** and **2**). Curiously, BLLs, subdivided into four subclasses, and FSRQs differ significantly in their radio, optical, and high-energy properties and can be arranged in a sequence (see Fossati et al. 1998, figure 5). In the radio, the BLL magnetic field is perpendicular to the projected jet axis, even when the jet bends; the FSRQ magnetic field is either aligned or random (Gabuzda 2014). This is argued to imply that BLL jets contain a strong, helical magnetic field, while the emission from FSRQs are dominated by either turbulent or laminar shear flows (Hughes et al. 1989).

We have contrasted leptonic and hadronic models of the γ-ray peak in FSRQs (Sections 2.3, 4.2.2.6, and 4.2.2.7) and argued that the latter may be able to account for rapid GeV variability if a disk outflow can shield the jet efficiently. This strongly suggests that we identify quasar broad emission lines with clouds driven away from the disk (Emmering et al. 1992, Königl & Kartje 1994, Bottorff et al. 1997), an interpretation that should be testable. By contrast, in the BLLs, the low density of optical and infrared photons allows protons to be accelerated to higher energy, emitting TeV photons that can now escape from small radii without strong shielding. The discovery of TeV emission from FSRQs with minute-scale variability would exclude this model.

5.4. Environmental Impact

AGN jets heat their galactic surroundings—efficiently in the case of FR-I sources and rather inefficiently in the case of the more powerful FR-II sources, which, instead, create hot cocoons that help protect jets from destructive instability (Fabian 2012). After the jet switches off or declines in power, these cocoons may detach to form giant bubbles that rise buoyantly away from the galaxy. They are ultimately assimilated by the circumgalactic medium, which they heat. This is most important when the host galaxies reside in a rich galaxy cluster. Jets can have a more immediate effect by stimulating star formation, as is sometimes seen in some galaxies, and, more impressively, by triggering the formation of new galaxies as the jets can propagate several megaparsecs away from their hosts. Jets also accelerate high-energy cosmic rays and quite plausibly may account for a large fraction of the universal spectrum above the knee in the spectrum. They may also be responsible for most of the intergalactic magnetic field.

So, AGNs play a major role in the evolution of the Universe, arguably comparable to that played by stars, and the jets can mediate this interaction directly. Quantitative measures of this role are still quite uncertain and must be compared with the influence of the radiation and outflowing winds that are associated with the accretion disks. All of this must be considered in the young Universe, when most nuclear activity occurred and massive black holes grew, and even earlier, when the intergalactic medium was reionized and the first stars and galaxies were formed. We

therefore conclude this article with a sketchy overview of attempts to address some of these issues and relate clear taxonomic structure in the observed properties of radio sources to underlying physical processes.

5.4.1. Cosmological evolution of extragalactic jets. Ever since radio sources were first identified with optical sources (galaxies and quasars) of moderate and high redshift, it has been obvious that the radio source population was quite different at early cosmological times than at present (Pooley & Ryle 1967, Schmidt 1968, Rees 1971). As beautifully shown by Wall et al. (1977), when source counts, local radio luminosity function, and redshift data are combined, it is clear that the bright (FR-II) end of the luminosity function was the much more populous one in the past. At the present epoch powerful radio sources and quasars are rather rare.

As shown above, the jet powers generated by both accretion disks and rotating black holes are an increasing function of the black hole feeding rate $\dot{m}$. Furthermore, a large body of work in the fields of coevolution of black holes and galaxy growth have tied the star formation rate closely to the long-term feeding rate of the central hole, both of which are believed to be driven ultimately by the rate of galaxy-galaxy mergers (Ho 2004, Padovani 2016). A plausible explanation for the decrease in activity of powerful radio sources over time, therefore, is the decrease in galaxy merger rate over that same time. Much work has been done on computational studies of large cosmological volumes of galaxy formation and merging. However, given all the complex processes at work, our understanding of the evolution of AGN jets will continue to be led by the results of large surveys.

5.4.2. Radio source lifetimes and duty cycle. The term "lifetime" can refer to at least three different timescales for radio sources: (*a*) The radiative lifetime is the period in which all the energy in the source lobes would be radiated away at its present luminosity. (*b*) The engine lifetime is the period during which the black hole spins rapidly and/or is being fueled sufficiently. The absence of orphaned lobes (Section 4.3.5) implies that the engine lifetime must be somewhat longer than the lobe radiative lifetime in most sources. (*c*) The cycle time is the period between engine outbursts for given radio source, during which jet production is dormant.

It is probably the case that each radio galaxy goes through different luminosity stages in its history. For example, M87 was probably a powerful FR-II galaxy in early cosmic times but eventually became the weak FR-I radio galaxy it is today. Therefore, actual values of the three above timescales make sense only when specified for a given radio source class. For example, the radiative lifetime of FR-II sources is $\sim 10^{6-7}$ years (O'Dea 2002), while the maximum engine lifetime (as measured by estimating the maximum FR-II lobe expansion and dissipation time in galaxy groups and clusters) is $\sim 1.7 \times 10^7$ years (Bird et al. 2008). These authors also estimated the time between each engine-fueling episode to be $\sim 10^9$ years. So, powerful radio source engines seem to produce a jet for $\lesssim 17$ Myr, but can be retriggered every 1 Gyr or so, with a duty cycle of $<2\%$.

In the case of most FR-I sources, the number density of these low-power radio galaxies does not appear to evolve much with cosmic time (Schmidt 1972). That is, the population evolutionary timescale for FR-Is is very long—greater than the age of the Universe. This suggests that the engine fueling may be essentially continuous for FR-Is, but at a low rate.

6. SUMMARY

> . . .direct studies of the event horizon shadow of supermassive black hole candidates are now possible via electromagnetic waves, thus transforming this elusive boundary from a mathematical concept to a physical entity. . .
>
> —K. Akiyama et al. (2019a, p. L9)

6.1. Toward a Working Model of AGN Jets

Relativistic jets are the conduits that connect supermassive, spinning black holes and their attendant disks to their host galaxies and the Universe beyond. They were once seen as exhausts that, like their automotive counterparts, remove excess heat from powerful machines. However, the observations that we have reviewed suggest a rather different metaphor. Black holes are turbines that are spun up by orbiting gas to generate high-voltage electrical power, and AGN jets are lossy, glowing coaxial cables that ultimately heat their surroundings. This change of viewpoint is supported by observations of selected local AGNs, from which we tentatively generalize to AGNs in general.

Nonetheless, this view suggests causal and testable mechanisms through which the type of AGN that is produced is determined by the black hole mass, spin, gas supply rate, and strength of the magnetic field, which in turn may depend upon the manner by which gas is supplied to the nucleus at $R_{\rm inf}$. In particular, it appears that only powerful jets can escape the nucleus as supersonic, relativistic flows. This model also suggests that AGN jets can accelerate protons to EeV energy and that they could be significant sources of high-energy cosmic rays. This further allows jet γ-ray emission to be mostly synchrotron instead of Compton radiation. In toto, AGNs contribute to and are constrained by the γ-ray background (Di Mauro et. al. 2018). Understanding the content, power, electrical current, and duty cycles of AGN jets will help quantify their role in galaxy formation and evolution.

6.2. Observing AGN Jets with New Telescopes

These are exciting times in the study of AGN jets. Our understanding of how they operate and how they relate to other manifestations of nuclear activity has matured over the past decade through the opening up of the γ-ray spectrum, the development of millimeter VLBI, and the systematic, multiwavelength study of large samples. High-dynamic-range RMHD and PIC simulations have also solidified our basic physical understanding of how black holes and their disks release energy and how their coronae, winds, and jets accelerate particles to impressive energies. While many questions remain, the prospects are good for obtaining clean answers soon because several new observational facilities are coming online.

The most immediate of these is EHT. This is making millimeter—and eventually attempting submillimeter—images with limiting angular resolution of a few gravitational radii in the best-resolved cases led by M87 and SgrA* so that general relativistic optics will be necessary to measure the black hole masses and spins and to interpret the images. The EHT M87 observations (see Sections 2.2.3.1, 3.1.2 and **Figure 1**) support the view that massive black holes, with a low gas supply, are embedded in a strong magnetic field confined by a much larger ejection disk (see the sidebar Classical and Revisionist Accretion Disk Theory) of orbiting gas, and their jets are powered by black hole spin, not accretion. The nature of the SgrA* source should also be revealed, and a weak jet will be either detected or bounded. A larger sample of sources will be used to determine if the model of the M87 black hole jet region is more widely applicable. Similar scales are being probed by the GRAVITY instrument deployed on the Very Large Telescope, which has reported strong astrometric and polarimetric evidence for features orbiting the SgrA* black hole close to the ISCO (Abuter et al 2018).

In the optical and infrared bands, the *James Webb Space Telescope* (2021), Giant Magellan Telescope (2023), Extremely Large Telescope (2024), and Thirty Meter Telescope (2027) will observe the inner parts of galaxies with angular resolution of ∼100 mas at 2 μm. The *James Webb Space Telescope* will have a far greater sensitivity, but ground-based telescopes can improve the angular resolution by nearly an order of magnitude using adaptive optics. Together these telescopes should be able to resolve galaxy jets and define both the gravitational potential and the ISM within $R_{\rm inf}$

through which they propagate. They will also help understand the flow of gas, both inward and outward, and how it relates to accretion, in addition to revealing some of the impact a powerful jet can have on its environment.

The Cherenkov Telescope Array comprises two observatories in Chile and La Palma and should begin construction in 2019 to be fully operational in the middle of the next decade. It will have ten times the sensitivity of existing telescopes, an improved energy coverage from ∼30 GeV to ∼100 TeV, angular resolution up to ∼3′ at high energy, and much better time coverage of the most prominent sources than previous instruments. It should greatly improve our understanding of jet beaming and variability and help us determine the geometry, speeds, and emission mechanisms of black hole jets. The Large High Altitude Air Shower Observatory will use water Cerenkov detectors to extend the gamma range to ∼1 PeV.

In the X-ray band, the Imaging X-ray Polarimetry Explorer should be able to detect many more X-ray blazars and learn about their magnetic field structure and, on a longer timescale, the Advanced Telescope for High Energy Astrophysics will improve on existing telescopes in sensitivity and resolution.

The long-term future of radio astronomy is defined by the Square Kilometer Array project and the Next Generation Very Large Array proposal. Collectively, these undertakings, with their precursors and pathfinders, advertise up to fifty times the sensitivity of existing radio telescopes from 50 MHz to 116 GHz. They will also greatly improve the sensitivity of centimeter-wavelength VLBI. They will be able to observe very large samples of extragalactic radio sources and map their black hole jets so as to develop a much better statistical understanding of beaming and structure on parsec scales.

Many more telescopes will be combined with these facilities, working in multiwavelength/messenger mode. Collectively, they are confidently expected to make discoveries that will advance the scientific program from the following list of goals tentatively suggested by this review.

6.3. Some Future Challenges

We conclude with a list of specific scientific challenges that we believe should be addressable using these facilities:

- Discover new information about gas flow and jet production around black holes using millimeter and submillimeter EHT observations
- Understand if the sustenance of a magnetic field near a black hole, which determines whether an AGN is radio loud or radio quiet, is due to physical processes near the black hole or controlled by the infalling gas
- Employ VHE neutrino observations to open up a new window on AGNs and determine if blazar jets are major cosmic ray sources
- Use EHT to study many jets on the scale of $R_{\rm inf}$ and verify that the FR class of a radio source is determined here
- Learn how to map emission in a given spectral band onto jet radius
- Determine if the TeV emission from blazars is synchrotron or Compton radiation
- Develop hybrid numerical simulations that meld relativistic hydromagnetic descriptions with particle kinetics and radiative transfer
- Quantify the role of AGN jets in promoting and limiting galaxy formation and evolution

DISCLOSURE STATEMENT

The authors are not aware of any affiliations, memberships, funding, or financial holdings that might be perceived as affecting the objectivity of this review.

ACKNOWLEDGMENTS

We thank Ramesh Narayan for his careful and constructive review of the first draft of this article and Noemie Globus for a careful reading of the revised draft. Beyond this, our debt and gratitude to more colleagues than we can possibly list, who have framed our evolving views on AGN jets over the past fifty years, are deep and sincere.

LITERATURE CITED

Aartsen MG, Abraham K, Ackermann M, et al. 2017. *Ap. J.* 835:45–62
Abdo AA, Ackermann M, Ajello, et al. 2011. *Ap. J.* 736:131–52
Abeysekara AU, Albert A, Alfaro R, et al. 2018. *Nature* 562:82–85
Abramowicz MA, Fragile PC. 2013. *Living Rev. Relativ.* 16:1–88
Abuter R, Amorim A, Bauböck M, et al. 2018. *Astron. Astrophys.* 618:L10–L24
Ackermann M, Ajello M, Atwood WB, et al. 2015. *Ap. J.* 810:14–48
Ackermann M, Anantua R, Asano K, et al. 2016. *Ap. J.* 824:L20–24
Ajello M, Romani RW, Gasparrini D, et al. 2014. *Ap. J.* 780:73–96
Akiyama K, Alberdi A, Alef W, et al. 2019a. *Ap. J.* 875:L1
Akiyama K, Alberdi A, Alef W, et al. 2019b. *Ap. J.* 875:L5
Algaba JC, Nakamura M, Asada K, Lee SS. 2017. *Ap. J.* 834:65–75
Aller MF, Aller HD, Hughes PA. 2017. *Galaxies* 5:75–94
Antonucci RRJ, Miller J. 1985. *Ap. J.* 297:621–32
Araudo AT, Bell AR, Blundell KM, Matthews JH. 2018. *MNRAS* 473:3500–6
Asada K, Nakamura M. 2012. *Ap. J.* 745:L28–32
Asada K, Nakamura M, Doi A, Nagai H, Inoue M. 2014. *Ap. J.* 781:L2–6
Avachat SS, Perlman ES, Sparks WB, et al. 2015. In *Proceedings, IAU Symposium 313: Extragalactic Jets from Every Angle*, ed. F Massaro, CC Cheng, D Lopez, A Siemiginowska, pp. 116–21. Cambridge, UK: Cambridge Univ. Press
Baade W, Minkowski R. 1954. *Ap. J.* 119:206–14
Balbus SA, Hawley JF. 1998. *Rev. Mod. Phys.* 70:1–53
Balick B, Brown R. 1974. *Ap. J.* 194:265–70
Bally J. 2016. *Annu. Rev. Astron. Astrophys.* 54:491–528
Balokovic M, Paneque D, Madejski G, et al. 2016. *Ap. J.* 819:156–86
Bardeen JM. 1970. *Nature* 226:64–65
Barniol Duran R, Tchekhovskoy A, Giannios D. 2017. *MNRAS* 469:4957–78
Barvainis R, Lehár J, Birkinshaw M, et al. 2005. *Ap. J.* 618:108–22
Beasley AJ, Gordon D, Peck AB, et al. 2002. *Ap. J.* 141:13–21
Bednarek W. 1997. *MNRAS* 285:69–81
Begelman MC. 1998. *Ap. J.* 493:291–300
Begelman MC, Blandford RD, Rees MJ. 1984. *Rev. Mod. Phys.* 56:255–351
Begelman MC, Ergun RE, Rees MJ. 2005. *Ap. J.* 625:51–59
Bellido J, Pierre Auger Collab. 2018. In *Proceedings of the 35th International Cosmic Ray Conference*, artic. 506. Trieste, Italy: Proc. Sci.
Beloborodov AM. 2017. *Ap. J.* 850:141–51
Bicknell GV. 1995. *Ap. J. Suppl.* 101:29–39
Bicknell GV, Begelman MC. 1996. *Ap. J.* 467:597–621
Bignami GF, Bennett K, Buccheri R, et al. 1981. *Astron. Astrophys.* 93:71–75
Bird J, Martini P, Kaiser C. 2008. *Ap. J.* 676:147–62
Biretta JA, Sparks W, Macchetto F. 1999. *Ap. J.* 520:621–26
Blandford RD. 1976. *MNRAS* 176:465–81
Blandford RD, Begelman MC. 1999. *MNRAS* 303:L1–5
Blandford RD, Königl A. 1979. *Ap. J.* 232:34–48
Blandford RD, Payne DG. 1982. *MNRAS* 199:883–903

Blandford RD, Rees MJ. 1974. *MNRAS* 169:395–415
Blandford RD, Rees MJ. 1978. In *Pittsburgh Conference on BL Lac Objects*, ed. AM Wolfe, pp. 328–47. Pittsburgh, PA: Univ. Pittsbg. Press
Blandford RD, Yuan Y, Hoshino M, Sironi L. 2017. *Space Sci. Rev.* 207:291–317
Blandford RD, Znajek RL. 1977. *MNRAS* 179:433–56
Blinov D, Pavlidou V, Papadakis I, et al. 2018. *MNRAS* 474:1296–306
Boccardi B, Krichbaum TP, Ros E, Zensus JA. 2017. *Astron. Astrophys. Rev.* 25:4–5
Bondi H. 1952. *MNRAS* 112:195–204
Böttcher M, Reimer A, Zhang H. 2013. In *Proceedings of The Innermost Regions of Relativistic Jets and Their Magnetic Fields*, ed. JL Gomez, artic. 05003. London: EDP Sci.
Bottorff M, Koroista KT, Shlosman I, Blandford RD. 1997. *Ap. J.* 479:200–21
Brandt WN, Alexander DM. 2015. *Astron. Astrophys. Rev.* 23:1–93
Braun PS. 2012. *Adv. Space Res.* 50:96–100
Bridle AH, Perley RA. 1984. *Annu. Rev. Astron. Astrophys.* 22:319–58
Burbidge GR. 1956. *Ap. J.* 124:416–29
Campbell WW, Moore JH. 1918. *Publ. Lick Obs.* 13:75–184
Chen AY, Yuan Y, Yang H. 2018. *Ap. J.* 863:L31–36
Cheung CC, Harris DE, Stawarz L. 2007. *Ap. J.* 663:L65–68
Clarke DA, Norman ML, Burns JO. 1986. *Ap. J.* 311:L63–67
Clautice D, Perlman ES, Georganopoulos M. 2016. *Ap. J.* 826:109–21
Cohen MH, Aller HD, Aller MF, et al. 2018. *Ap. J.* 862:1–18
Cohen MH, Canon W, Purcell GH, et al. 1971. *Ap. J.* 170:207–17
Cohen MH, Kellermann KI, Shaffer DB, et al. 1977. *Nature* 268:405–9
Cohen MH, Meier DL, Arshakian TG, et al. 2014. *Ap. J.* 787:151–60
Cohen MH, Meier DL, Arshakian TG, et al. 2015. *Ap. J.* 803:3–18
Contopoulos I, Nathanail N, Sadowski A, et al. 2018. *MNRAS* 473:721–27
Curtis HD. 1918. *Publ. Lick Obs.* 13:9–42
De Villiers J-P, Hawley JF. 2003. *Ap. J.* 589:458–80
De Young DS. 1993. *Ap. J.* 405:L13–16
Dent WA. 1965. *Science* 148:1458–60
Di Mauro M, Manconi S, Zechlin H-S, et al. 2018. *Ap. J.* 856:106–18
Doeleman SS. 2012. *Science* 361:848–49
Doeleman SS, Fish VL, Schenk DE, et al. 2012. *Science* 338:355–58
Drury LO'C. 1983. *Rep. Prog. Phys.* 46:973–1027
Durant M, Kargaltsev O, Pavlov GG, et al. 2013. *Ap. J.* 763:72–76
EHT (Event Horizon Telesc.) Collab. 2019. *Ap. J. Lett.* 875:L1
Elvis M, Risaliti G, Zamorani G. 2002. *Ap. J.* 565:L75–77
Emmering RT, Blandford RD, Shlosman I. 1992. *Ap. J.* 385:460–77
Fabian AC. 2012. *Annu. Rev. Astron. Astrophys.* 50:455–89
Fanaroff BL, Riley JM. 1974. *MNRAS* 167:31P–36P
Fath EA. 1909. *Publ. Astron. Soc. Pac.* 17:504–8
Fender RP, Belloni TM, Gallo E. 2004. *MNRAS* 355:1105–18
Fossati G, Maraschi L, Celotti A, et al. 1998. *MNRAS* 299:433–48
Fuhrmann L, Larsson S, Chang J, et al. 2014. *MNRAS* 441:1899–909
Funk S. 2014. *Annu. Rev. Nucl. Part. Sci.* 65:245–77
Gabuzda DC. 2014. In *The Formation and Disruption of Black Hole Jets*, ed. I Contopoulos, D Gabuzda, N Kylafis, pp. 117–48. Heidelberg, Ger.: Springer
Gabuzda DC, Murray É, Cronin P, et al. 2004. *MNRAS* 351:L89–93
Gabuzda DC, Roche N, Kirwan A, et al. 2017. *MNRAS* 472:1792–801
Gammie CF, McKinney JC, Tóth G. 2003. *Ap. J.* 589:444–57
Garrington ST, Leahy JP, Conway RG, et al. 1988. *Nature* 331:147–49
Gehrels N, Ramirez-Ruiz E, Fox DB. 2009. *Annu. Rev. Astron. Astrophys.* 47:567–617

Georganopoulos M, Meyer ET, Perlman ES. 2017. *Galaxies* 4:65–73
Ghisellini G. 2016. *Galaxies* 4:36–46
Ghisellini G, Celotti A, Fossti G, et al. 1998. *MNRAS* 301:451–68
Giovannini G, Savolainen T, Orienti M, et al. 2018. *Nat. Astron.* 2:472–7
Giroletti M, Hada K, Giovannini G, et al. 2012. *Astron. Astrophys.* 538:L10–13
Globus N, Levinson A. 2016. *MNRAS* 461:2605–15
Globus N, Piran T, Hoffman Y, Carlesi E, Pomarède D. 2019. *MNRAS* 484:4167–73
Gonzalez JB. 2015. In *Astrophysical Jets from Every Angle*, ed. F Massaro, CC Cheng, D Lopez, A Siemiginowska, pp. 64–69. Cambridge, UK: Cambridge Univ. Press
Gopal-Krishna, Wiita PJ. 2000. *Astron. Astrophys.* 363:507–16
Gubbay J, Legg AJ, Robertson DS, et al. 1969. *Nature* 224:1094–95
Gugliucci NE, Taylor GB, Peck AB, Giroletti M. 2005. *Ap. J.* 622:136–48
Hada K, Giroletti M, Kino M, et al. 2014. *Ap. J.* 788:165–77
Hargrave P, Ryle M. 1974. *MNRAS* 166:305–27
Harris DE, Krawczynski H. 2006. *Annu. Rev. Astron. Astrophys.* 44:463–506
Hayashida M, Madejski GM, Nalewajko K, et al. 2012. *Ap. J.* 754:114–36
Hazard C, Mackey MB, Shimmins AJ. 1963. *Nature* 197:1037–39
Hillas AM. 1984. *Annu. Rev. Astron. Astrophys.* 22:425–44
Hine RG, Longair MS. 1979. *MNRAS* 188:111–30
Ho LC, ed. 2004. *Coevolution of Black Holes and Galaxies*. Cambridge, UK: Cambridge Univ. Press
Hodgson JA, Ranu B, Lee S-S, et al. 2018. arXiv:1802.02763 [astro-ph.HE]
Homan DC, Hovatta T, Kovalev Y, et al. 2018. *Galaxies* 6:17–24
Homan DC, Lister ML. 2006. *Ap. J.* 131:1262–79
Hovatta T, Lister ML, Aller MF, et al. 2012. *Astron. J.* 144:105–39
Hoyle F, Burbidge GR, Sargent WLW. 1966. *Nature* 209:751–53
Hughes MP. 1965. *Nature* 207:178–79
Hughes PA, Aller HD, Aller MF. 1989. *Ap. J.* 341:54–67
IceCube Collab. 2018. *Science* 361:147–51
Ivezić Z, Menou K, Knapp GR, et al. 2002. *Astron. J.* 124:2364–400
Jackson CA, Wall JV. 1999. *MNRAS* 304:160–74
Jansky KG. 1933. *Nature* 132:66
Jauncey D, Bignall H, Kedziora-Chudzer L, et al. 2016. *Galaxies* 4:62–71
Jennison RC, Das Gupta MK. 1953. *Nature* 172:996–97
Jorstad S, Marscher A. 2016. *Galaxies* 4:47–57
Jorstad SG, Marscher AP, Mattox JR, et al. 2001. *Ap. J.* 556:738–48
Karouzos M, Britzen S, Witzel A, et al. 1983. *Astron. Astrophys.* 529:A16–28
Keel WC. 1983. *Ap. J.* 269:466–86
Kellermann KI, Condon JJ, Kimball AE, et al. 2016. *Ap. J.* 831:168–80
Kellermann KI, Pauliny-Toth IIK. 1969. *Ap. J.* 155:L71–78
Kerr RP. 1963. *Phys. Rev. Lett.* 11:237–38
Kharb P, Stanley E, Lister M, et al. 2014. In *Proceedings, IAU Symposium 313: Extragalactic Jets from Every Angle*, ed. F Massaro, CC Cheng, D Lopez, A Siemiginowska, pp. 211–18. Cambridge, UK: Cambridge Univ. Press
Kim J-Y, Krichbaum TP, Lu R-S, et al. 2018. *Astron. Astrophys.* 616:A188–201
Kim J-Y, Krichbaum TP, Marscher AP, et al. 2019. *Astron. Astrophys.* 622:196–214
King A, Pounds K. 2015. *Annu. Rev. Astron. Astrophys.* 53:115–54
Königl A. 1981. *Ap. J.* 243:700–9
Königl A, Kartje JF. 1994. *Ap. J.* 434:446–67
Kormendy J, Ho LC. 2013. *Annu. Rev. Astron. Astrophys.* 51:511–653
Kulsrud RM. 2004. *Plasma Physics for Astrophysics*. Princeton, NJ: Princeton Univ. Press
Laing RA. 1996. In *Energy Transport in Radio Galaxies and Quasars*, ed. PE Hardee, AH Bridle, JA Zensus, pp. 241–52. San Francisco: Publ. Astron. Soc. Pac.

Laing RA, Bridle AH. 2014. *MNRAS* 437:3405–41
Landau LD, Lifshitz EM. 1975. *The Classical Theory of Fields*. Oxford, UK: Butterworth-Heinemann
Lauer RJ. 2015. In *Proceedings, IAU Symposium 313: Extragalactic Jets from Every Angle*, ed. F Massaro, CC Cheng, D Lopez, A Siemiginowska, pp. 27–32. Cambridge, UK: Cambridge Univ. Press
Levinson A, Blandford R. 1995. *MNRAS* 274:717–29
Levinson A, Globus N. 2017. *MNRAS* 465:1608–12
Levinson A, Segev N. 2017. *Phys. Rev. D.* 96:123006–19
Lind KR, Payne DG, Meier DL, Blandford RD. 1989. *Ap. J.* 344:89–103
Lindfors E. 2015. In *Proceedings, IAU Symposium 313: Extragalactic Jets from Every Angle*, ed. F Massaro, CC Cheng, D Lopez, A Siemiginowska, pp. 27–32. Cambridge, UK: Cambridge Univ. Press
Lister ML. 2016. *Galaxies* 4:29–38
Lister ML, Aller MF, Aller HD, et al. 2016. *Astron. J.* 152:1–16
Longair MS. 2011. *High Energy Astrophysics*. Cambridge, UK: Cambridge Univ. Press
Lott B, Cavazzuti E, Ciprini S, et al. 2015. In *Extragalactic Jets from Every Angle*, ed. F Massaro, CC Cheng, D Lopez, A Siemiginowska, pp. 11–16. Cambridge, UK: Cambridge Univ. Press
Lovelace RVE. 1976. *Nature* 262:649–52
Lynden-Bell D. 1969. *Nature* 223:690–94
Madejski GM, Sikora M. 2016. *Annu. Rev. Astron. Astrophys.* 54:725–60
Madsen KK, Fürst F, Walton D, et al. 2015. *Ap. J.* 812:14–25
Marscher AP. 2014. *Ap. J.* 780:87–96
Marscher AP, Jorstad SG, D'Arcangelo FD, et al. 2008. *Nature* 452:966–69
Marscher A, Jorstad SG, Larionov VM, et al. 2011. *J. Astrophys. Astron.* 32:233–37
Marshall HL, Miller BP, Davis DS. 2002. *Ap. J.* 564:683–87
Matthews JH, Bell AR, Blundell KM, Araudo AT. 2018. *MNRAS* 479:L76–80
Max-Moerbeck W, Hovatta T, Richards JL, et al. 2014. *MNRAS* 445:428–36
McKinney JC. 2006. *MNRAS* 368:1561–82
McKinney JC, Dai M, Avara MJ. 2015. *MNRAS* 411:L6–10
McKinney JC, Narayan R. 2007. *MNRAS* 375:531–47
McKinney JC, Tchekhovskoy A, Blandford RD. 2012. *MNRAS* 423:3083–117
McKinney JC, Tchekhovskoy A, Sadowski A, Narayan R. 2014. *MNRAS* 441:3177–208
Meier DL. 2012. *Black Hole Astrophysics: The Engine Paradigm*. Berlin: Springer
Meier DL. 2013. In *Proceedings of The Innermost Regions of Relativistic Jets and Their Magnetic Fields*, ed. JL Gomez. London: EDP Sci.
Mertens F, Lobanov AP, Walker RC, Hardee PE. 2016. *Astron. Astrophys.* 595:A54–73
Meyer M, Scargle JD, Blandford RD. 2019. *Ap. J.* 877:1
Mignone A, Rossi P, Bodo G, et al. 2010. *MNRAS* 402:7–12
Mirabel IF, Rodriguez LF. 1999. *Annu. Rev. Astron. Astrophys.* 37:409–43
Mooley KP, Deller AT, Gottlieb O, et al. 2018. *Nature* 7723:355–9
Muecke A, Protheroe RJ, Engel R, et al. 2003. *Astropart. Phys.* 18:593–613
Nakamura M, Asada K. 2013. *Ap. J.* 775:118–28
Nakamura M, Asada K, Hada K, et al. 2018. *Ap. J.* 868:146–73
Nakamura M, Garofalo D, Meier DL. 2010. *Ap. J.* 721:1783–89
Nakamura M, Meier DL. 2004. *Ap. J.* 617:123–54
Nalewajko K, Begelman MC, Sikora M. 2014. *Ap. J.* 789:161–80
Narayan R, Igumenschev IV, Abramowicz MA. 2003. *Publ. Astron. Soc. Jpn.* 55:L69–72
Narayan R, McClintock JE. 2012. *MNRAS* 419:L69–73
Norman ML, Winckler K-HA, Smarr LL, Smith MD. 1982. *Astron. Astrophys.* 113:285–302
O'Dea CP. 2002. *New Astron. Rev.* 46:41–46
Orr MJL, Browne IWA. 1982. *MNRAS* 200:1067–80
Osterbrock DE, Ferland GJ. 2005. *Astrophysics of Gaseous Nebulae and Active Galactic Nuclei*. Mill Valley, CA: Univ. Sci.
Padovani P. 2016. *Astron. Astrophys. Rev.* 24:13–48

Pauliny-Toth IIK, Witzel A, Preuss E, et al. 1978. *Astron. J.* 83:451–74
Penna RF, Narayan R, Sadowski A. 2013. *MNRAS* 436:3741–58
Penrose R. 1969. *Riv. Nuovo Cim.* 1:252–76
Petropoulou M, Mastichiadis A. 2012. *MNRAS* 426:462–72
Petrov L. 2017. *Trans. Inst. Appl. Astron. Russ. Acad. Sci.* 40:64-67
Petrov L, Phillips C, Bertarini A, et al. 2011. *MNRAS* 414:2528–39
Plavin AV, Kovalelv YY, Pushkarev AB, Lobanov AP. 2018. arXiv:1811.02544v1 [astro-ph.GA]
Pooley GG, Ryle M. 1967. *MNRAS* 139:515–28
Potter WJ. 2018. *MNRAS* 473:4107–21
Potter WJ, Cotter G. 2015. *MNRAS* 453:4070–88
Prandini E. 2017. arXiv:1706.01670v2 [astro-ph.HE]
Prieto MA, Fernandez-Ontiveros JA, Markoff S, Espada D, González-Martin O. 2016. *MNRAS* 457:3801–16
Punch M, Akerlof CW, Cawley MF, et al. 1992. *Nature* 358:477–78
Pushkarev A, Kovalev Y, Lister M, et al. 2017. *Galaxies* 5:93–99
Qian Q, Fendt C, Vourellis C. 2018. *Ap. J.* 859:28–51
Rani B, Jorstad SG, Marscher AP, et al. 2018. *Ap. J.* 858:80–95
Rani P, Stalin CS, Rakshit S, et al. 2017. *MNRAS* 466:3309–22
Readhead ACS. 1980. In *Objects of High Redshift*, ed. GO Abell, PJE Peebles, pp. 165–76. Dordrecht, Neth.: Reidel
Readhead ACS. 1994. *Ap. J.* 426:51–59
Readhead ACS, Cohen MH, Blandford RD. 1978. *Nature* 272:131–34
Readhead ACS, Cohen MH, Pearson TJ, Wilkinson PN. 1978. *Nature* 276:768–71
Readhead ACS, Taylor GB, Xu W, et al. 1996. *Ap. J.* 460:612–33
Readhead ACS, Wilkinson PN. 1978. *Ap. J.* 223:25–36
Reber G. 1940. *Ap. J.* 91:621
Rees MJ. 1966. *Nature* 211:468–70
Rees MJ. 1967. *MNRAS* 135:345–60
Rees MJ. 1971. *Nature* 229:312–17
Rees MJ. 1984. *Annu. Rev. Astron. Astrophys.* 22:471–506
Rees MJ, Schmidt M. 1971. *MNRAS* 154:1–7
Reimer A. 2012. *J. Phys. Conf. Ser.* 355:12011–22
Reynolds CS. 2014. *Space Sci. Rev.* 183:277–94
Richards JL, Max-Moerbeck W, Pavlidou V, et al. 2011. *Ap. J. Suppl.* 194:29–51
Rybicki G, Lightman A. 1979. *Radiative Processes in Astrophysics*. New York: Wiley
Sadowski A, Narayan R. 2015. *MNRAS* 453:3213
Sadowski A, Narayan R, MacKinney JF, Tchekhovskoy A. 2014. *MNRAS* 439:503–20
Salpeter EE. 1964. *Ap. J.* 140:796–80
Sambruna R, Harris DE. 2012. In *Relativistic Jets from Active Galactic Nuclei*, ed. M Boettcher, DE Harris, H Krawczynski, pp. 185–214. New York: Wiley
Sandage A. 1965. *Ap. J.* 141:1560–78
Scheuer PAG. 1974. *MNRAS* 166:513–28
Scheuer PAG. 1982. In *Extragalactic Radio Sources*, ed. DS Heeschen, CM Wade, pp. 163–65. Dordrecht, Neth.: Reidel
Schmidt M. 1963. *Nature* 197:1040
Schmidt M. 1968. *Ap. J.* 151:393–409
Schmidt M. 1972. *Ap. J.* 176:289–301
Schreier EJ, Gorenstein P, Feigelson ED. 1982. *Ap. J.* 261:42–50
Schwartz D, Marshall H, Worrall D, et al. 2015. In *Proceedings, IAU Symposium 313: Extragalactic Jets from Every Angle*, ed. F Massaro, CC Cheng, D Lopez, A Siemiginowska, pp. 219–24. Cambridge, UK: Cambridge Univ. Press
Seyfert CK. 1943. *Ap. J.* 97:28–41
Shakura NI, Sunyaev RA. 1973. *Astron. Astrophys.* 24:337–55

Shklovsky IS. 1955. *Astron. J. USSR* 32:215–25
Sironi L, Spitkovsky A. 2014. *Ap. J.* 783:L21–26
Smith HJ, Hoffleit D. 1963. *Nature* 198:650–51
Sol H, Pelletier G, Asseo E. 1989. *MNRAS* 237:411–29
Soltan A. 1982. *MNRAS* 200:115–22
Stawarz L, Petrosian V. 2008. *Ap. J.* 681:1725–44
Tadhunter C. 2016. *Astron. Astrophys. Rev.* 24:10–68
Tavecchio F, Landoni M, Sironi L, Coppi P. 2018. *MNRAS* 480:2872–80
Tchekhovskoy A, Bromberg O. 2016. *MNRAS* 461:L46–50
Tchekhovskoy A, McKinney JC. 2012. *MNRAS* 423:L55–59
Tchekhovskoy A, Narayan R, McKinney JC. 2011. *MNRAS* 411:L79–83
Thompson TA, Quataert E, Murray N. 2005. *Ap. J.* 630:167–85
Thorne KS, Blandford RD. 2017. *Modern Classical Physics*. Princeton, NJ: Princeton Univ. Press
Titarchuk L, Seifinab E. 2017. *Astron. Astrophys.* 602:A113–28
Tremblay SE, Taylor GB, Ortiz AA, et al. 2016. *MNRAS* 459:820–40
Turland BD. 1975. *MNRAS* 172:181–89
Urry CM, Padovani P. 1995. *PASP* 107:803–45
Waggett PC, Warner PJ, Baldwin JE. 1977. *MNRAS* 181:465–74
Walker RC, Hardee PE, Davis FB, et al. 2018. *Ap. J.* 855:128–64
Wall JV, Pearson TJ, Longair MS. 1977. In *Radio Astronomy and Cosmology*, ed. DL Jauncey, pp. 269–78. Dordrecht, Neth.: Reidel
Walsh JL, Barth AJ, Ho LC, Sarzi M. 2013. *Ap. J.* 770:86–96
Wardle J. 2018. *Galaxies* 6:5–13
Werner GR, Uzdensky DA, Begelman MC, et al. 2018. *MNRAS* 473:4840–61
Werner MW, Murphy DW, Livingston JH, et al. 2012. *Ap. J.* 759:86–97
Whitney AR, Shapiro II,Rogers AEE, et al. 1971. *Science* 173:225–30
Wilkinson PN. 1995. *PNAS* 92:11342–47
Wilkinson PN, Polatidis AG, Readhead ACS, et al. 1994. *Ap. J.* 432:L87
Wilkinson PN, Readhead ACS, Purcell GH, Anderson B. 1977. *Nature* 269:764–8
Wolfe AM, ed. 1978. In *Pittsburgh Conference on BL Lac Objects*, ed. AM Wolfe, pp. 343–55. Pittsburgh, PA: Univ. Pittsbg. Press
Yu Q, Tremaine S. 2002. *MNRAS* 335:965–76
Yuan F, Narayan R. 2014. *Annu. Rev. Astron. Astrophys.* 52:555–88
Zavala RT, Taylor GB. 2004. *Ap. J.* 612:749–79
Zel'dovich YaB, Novikov ID. 1964. *Dokl. Acad. Nauk. SSSR* 155:1033–152
Zensus JA. 1997. *Annu. Rev. Astron. Astrophys.* 35:607–36
Zensus JA, Pearson TJ, eds. 1987. *Superluminal Radio Sources*. Cambridge, UK: Cambridge Univ. Press